The influence of pre-eruptive reservoir conditions on peralkaline magma explosivity: Case for the Rungwe Pumice (Tanzania) Plinian eruption

Lorenzo Cappelli - *Department of Geosciences, Environment and Society; Université libre de Bruxelles; Bruxelles, 1050, Belgium.* lorenzo.cappelli@ulb.be

Paul A. Wallace – *Department of Geosciences, Environment and Society; Université libre de Bruxelles; Bruxelles, 1050, Belgium.*

Department of Earth and Environmental Sciences; Ludwig-Maximilians-Universität München; München, 80539, Germany. Paul.Wallace@min.uni-muenchen.de

Evelyne Mbede – *School of Mines and Geosciences; University of Dar es Salaam; Dar es Salaam, 35052, Tanzania.* embede@gmail.com

Shimba Kwelwa – *AngloGold Ashanti; Geita, 532, Tanzania.* skwelwa750@gmail.com

Edista Abdallah – *School of Mines and Geosciences; University of Dar es Salaam; Dar es Salaam, 35052, Tanzania.* edisteralex@gmail.com

Gerald G.J. Ernst – no affiliation. plumeman2000@yahoo.co.uk

Karen Fontijn – *Department of Geosciences, Environment and Society; Université libre de Bruxelles; Bruxelles, 1050, Belgium.* karen.fontijn@ulb.be

Keywords: East African Rift; Melt Inclusions; Peralkaline magmas; Plinian-style eruptions; Storage conditions.

ABSTRACT

The style and explosivity of volcanic eruptions are primarily influenced by interrelated factors: conduit dynamics (such as magma ascent rate and degassing efficiency) and pre-eruptive magmatic conditions, both of which control the magma's rheological behaviour. In the case of highly alkaline magmas (i.e., agpaitic index > 1), the depolymerisation of silica bonds exerted by alkaline elements promotes a relatively low-viscosity rheological response for a given temperature and therefore theoretically less explosive eruptive behaviour, even for silica-rich magmas. However, several well-studied eruptions show that peralkaline magmas (e.g., trachytes or phonolites) can experience highly explosive Plinian events, suggesting other parameters influence eruption style. In the East African Rift, several such volcanoes with peralkaline magma compositions have erupted both explosively and effusively in the past. We investigated the pre-eruptive magmatic system of the Plinian eruption that produced the Rungwe Pumice (RP) deposit in southern Tanzania. The late chemical evolution of the plumbing system was modelled by analysing haüyne-hosted melt inclusions (MIs) which suggests that an evolved magmatic body of deeper origin was stored at shallow depths shortly before the eruption. Water concentrations in the MIs, measured using transmitted Fourier-transformed infrared spectroscopy, revealed water-poor conditions (e.g., 2-3 wt.%) and shallow depths (2-5 km). Thus, volatile concentration alone is not sufficient to explain the explosive behaviour, but the degree of water undersaturation and conduit dynamics must also be considered.

1 INTRODUCTION

The eruptive behaviour of magma is governed by the exsolution of volatiles and their efficiency in decoupling from the melt while rising in the volcanic conduit (Cassidy et al., 2018). Among other factors (e.g., ascent and thus decompression rate, conduit radius, the presence of crystals acting as nucleation sites), the efficiency of this process is strongly related to magma composition (i.e., major element and volatile concentrations) and the relative intrinsic rheology (Sparks, 1978; Degruyter et al., 2012 and references therein). A primary variable controlling explosivity is the availability of water dissolved in the melt, as this represents the engine of eruptions. The decompression of the melt at (approximately) isothermal conditions during magma ascent induces the oversaturation of volatiles, promoting the exsolution of a supercritical fluid and later gas phase that forms bubbles (vesicles) and will gradually turn the magma into a foam (Sparks, 1978). In turn, the viscosity of magma affects the diffusion of elements and volatile compounds inhibiting early bubble nucleation and, subsequently, slowing their uprising promoting vesicle-melt coupling. These processes may cause bubble overpressure and potential energy accumulation in the melt that will be released explosively when the decompression-related strain rate exceeds the structural relaxation timescales of the melt inducing brittle fragmentation (Dingwell and Webb, 1989; Dingwell, 1996; Cassidy et al., 2018).

Such eruptive dynamics, associated with polymerised high-silica magmas widespread along subduction-related, volcanic arcs, can produce violent Plinian-style eruptions. Elevated quantities of alkalis (Na and K) depolymerise the silica bonds of phonolitic or peralkaline trachytic and rhyolitic magmas resulting in melt viscosities that, at equivalent temperature and water content, are generally lower (by up to two orders of magnitude for rhyolite) than their calc-alkaline counterparts (Giordano et al., 2008; Di Genova et al., 2013). However, several well-known examples demonstrate that Plinian-style eruptions can also be generated from such

lower-viscosity, silica-undersaturated (e.g., Houghton et al., 2004; Jorgenson et al., 2024) or alkali-rich magmas (e.g., Cioni et al., 1999; White et al., 2012), even under water-undersaturated reservoir conditions (Andújar and Scaillet, 2012a). Interestingly, magmas with equivalent compositions can produce either effusive or explosive eruptions, even when erupting from the same volcano or during the same volcanic event (e.g., Aluto, Ethiopia; Hutchison et al., 2016). The eruptive dynamics that determine the shift between different eruptive styles remain a topic of ongoing debate. High-alkaline series magmas are overall less abundant on Earth than the calc-alkaline series. Still, they can be found in all geological settings, from subduction-related volcanic arcs to intraplate hotspots and they are particularly common in continental divergent settings, above all along the East African Rift (EAR).

Silicic volcanism within the EAR is characterised by extensive, multicentred volcanic systems whose Quaternary volcanism includes Plinian-size eruptions that sometimes culminated in caldera collapses (e.g., Williams et al., 1984; Macdonald, 1987; Fontijn et al., 2018). Magmatic products span from silica-undersaturated to -saturated compositions but are generally enriched in alkali elements. The limited knowledge of many of these volcanic centres leads to a substantial underestimation of the volcanic hazard in densely populated regions across the EAR (Biggs et al., 2021).

To unravel the factors influencing the explosivity of moderate viscosity, peralkaline systems widespread along the EAR, we investigated the pre-eruptive conditions of the Rungwe Pumice (RP) eruption. These parameters are critical indicators of the current state and potential unrest development of a magmatic reservoir. The RP is the result of a Plinian-style eruption generated by the Rungwe volcano in the Rungwe Volcanic Province (RVP; Tanzania). The eruption is dated around ~4 ka and occurred under near-wind-free conditions, producing a $\geq$1.4 km^3 dense rock equivalent pumice deposit radially distributed around the Rungwe summit (Fontijn et al., 2011). Information related to the pre-eruptive physical and chemical processes is well preserved

93 in crystal-hosted melt inclusions (MIs). These melt pockets, formed in crystal imperfections
94 during growth, can maintain chemical equilibrium with the original melt and are not affected
95 by its subsequent evolution during ascent (Esposito et al., 2014). MIs retain the original
96 concentrations of volatiles dissolved in the melt, whereas the pumice matrix melt extensively
97 degases upon ascent (e.g., Cioni, 2000). In this study, the evolution of magma chemistry and
98 water content within the pre-eruptive reservoir is analysed in haüyne-hosted MIs collected from
99 different stratigraphic horizons of a type section of the RP deposit. These findings were used to
100 evaluate the eruptive triggers and the role of water concentration in driving the eruptive style.

101 ## 2 RUNGWE VOLCANIC PROVINCE

102 The RVP covers more than 1500 km^2 and is located along the EAR in southern Tanzania (**Fig.**
103 **1**). The EAR is the largest divergent continental margin still active today. It is generated by the
104 divergence of the Somali and Nubian (African) Plates and extends south for over 3000 km from
105 the Afar triple junction to Mozambique (Saria et al., 2014). In its central part, the rift encounters
106 the thick and rigid Tanzanian craton and here it splits into two sectors termed Western and
107 Eastern branches (Saria et al., 2014; Ebinger et al., 2017). In the EAR the extension is driven
108 by gravitational stresses equilibrating the topographic anisotropy induced by the rising of the
109 African superplume and it is mostly accommodated by large border faults in the early stages of
110 rifting or by secondary, rift-floor faults and magmatic intrusions in more mature stages
111 (Keranen et al., 2004; Ebinger, 2005; Kendall and Lithgow-Bertelloni, 2016).

112 Volcanism is present across the entire rift but is predominantly concentrated in the more mature
113 Eastern branch (**Fig. 1a**). However, some of the present-day most active volcanic centres (e.g.,
114 Nyiragongo or Nyamuragira) can be found along the Western branch, where overall four of the
115 twenty-one EAR's volcanoes that erupted in historical times are located (Wadge et al., 2016).
116 The type of eruptive activity at EAR volcanoes spans from basaltic fissure eruptions and flood

basalts to Plinian, caldera-forming eruptions (Macdonald, 1987; Fontijn et al., 2011, 2018). Magmatic products range from mafic to silicic compositions along the alkaline or peralkaline series, and their genesis has been widely investigated (e.g., Macdonald and Scaillet, 2006; Hutchison et al., 2018).

The Rungwe Volcanic Province is located in the Western branch of the EAR, south of the Tanzanian Craton. Here, the Western branch deviates from the prevalent NW-SE trend of the Tanganyika-Rukwa rift toward the N-S trend of the North Malawi rift and also connects with the NE-SW trending Usangu basin (**Fig. 1a**). The RVP sits at the junction between the active Livingstone, Rukwa borders faults (Ebinger et al., 1993), which consistently controlled the spreading of volcanic centres (Fontijn et al., 2010a, 2012). Together with the main present-day active centres, Ngozi, Rungwe, and Kyejo, over 100 smaller eruptive centres are scattered across the area, and whose distribution follows two major NW-SE and NE-SW-oriented alignments (Fontijn et al., 2010a).

Volcanic stratigraphy reveals that the activity in the area commenced at around 9 Ma and was dominated by the eruption of basalts, trachytes and phonolites of alkaline composition, from both effusive and explosive eruptions (Fontijn et al., 2012 and references therein). According to field cross-correlation and radiometric ages of deposits, the activity has been divided into three main stages: 1) Late Miocene (9.2-5.4 Ma), 2) Late Pliocene-Early Pleistocene (3-1.6 Ma), 3) Mid-Pleistocene–Recent (since 0.6 Ma) (Fontijn et al., 2012 and references therein). The effusion of basaltic lava flows and the deposition of phonolitic ignimbrites dominate the first two stages. Many different volcanic centres, today buried or eroded, are considered the sources of these eruptions, possibly including the large Katete volcano (NE of Rungwe) and Tukuyu shield volcano (centred under Tukuyu town; Fontijn et al., 2012 and references therein). The last stage of activity commenced with basaltic and trachytic lava flows spreading northern in the Rukwa rift and Usangu basin and then concentrated into a narrow (~30 km-wide) NW-

SE trending sector of the RVP along the three main volcanic centres, Ngozi, Rungwe and Kyejo and their satellite small eruptive centres. During the second stage, the activity of several centres in the northern part built up Mporoto ridge, into which the Ngozi volcano was formed, and which culminated in the Late Pleistocene to Holocene (third stage) with large explosive eruptions (i.e., 10-12 ka Kitulo Pumice and < 1ka Ngozi Tuff) shaping its present-day caldera depression (Fontijn et al., 2010b). The edifice of the Kyejo volcano is composed of a multitude of small centres (*Kyejo cluster*; Fontijn et al., 2010a) that erupted effusively or mildly explosively. These satellite eruptive centres are scoria or spatter cones and mostly produced alkaline basaltic to trachytic-phonolitic lava flows (Harkin, 1960). The only historical eruption of the RVP belongs to the Kyejo cluster: the Sarabwe tephrite lava flow dated approximately 1800 CE from oral accounts (Fontijn et al., 2012). Beyond this, the volcanic history of Kyejo remains unknown.

Rungwe is the largest volcanic edifice in the RVP and is centrally located in the province (**Fig. 1b**). It consists of a stratovolcano structure whose summit is cut by a 300 m high scar facing WSW. The scar results from a sector collapse whose debris avalanche formed a hummocky landscape down to 22 km along the SW flank of the edifice (Fontijn et al., 2012). No evidence of associated magmatic activity exists for the gravitational collapse (Fontijn et al., 2012). The pre-collapse edifice is formed by lava flows of basaltic, phonolitic, and trachytic compositions, and the oldest dated unit has a whole-rock K-Ar age of 0.25 ± 0.01 Ma (Ebinger et al., 1989). Multiple silicic domes and tephra cones formed on the edifice summit depression after the sector collapse. The most relevant deposit that is widespread across the whole RVP is the ~4 ka old Rungwe Pumice (RP) deposit (Fontijn et al., 2010b, 2011). The latest activity of Rungwe includes the eruption of the Isongole Pumice, the second most explosive eruption of Rungwe (VEI 4; Newhall and Self, 1982), and three additional explosive eruptions of reduced intensity dated < 1.5 ka (i.e., Ngumbulu Tephra; Aphyric Pumice, Kizungu Tephra; Fontijn et al., 2010b).

Overall, a rate of at least one explosive eruption every 500 years is estimated for Rungwe volcano, including violent Strombolian to Plinian events (Fontijn et al., 2010b).

2.1 Rungwe Pumice eruption

The RP deposit consists of a massive pumice lapilli fall deposit that covers the RVP completely and is dated around 4 ka based on radiocarbon dating of the underlying palaeosol (Fontijn et al., 2010a) and age constraints from the Lake Masoko sedimentary record (Garcin et al., 2006). The deposit is lithic-poor and is predominantly composed of cream-coloured, highly vesiculated pumice lapilli of high-alkaline, trachytic composition (WR; Fontijn et al., 2013). Additionally, a small proportion (<1wt%) of grey/banded pumice was found and interpreted as indications of mingling with a slightly more mafic melt (Fontijn et al., 2011). In the finer grain-size ranges (≤1.5 mm), alkali feldspar is the main mineralogical component followed by subordinate amounts of biotite, clinopyroxene and Fe-Ti oxides. Of particular interest is the occurrence of cyan-coloured haüyne which is absent in most other deposits from the RVP. These crystals, clearly visible to the naked eye, have been used as a marker to track down RP outcrops in the field (Fontijn et al., 2011). More than 100 RP outcrops were mapped around the province up to 28 km from Rungwe summit, but where it still has a thickness of 30 cm. A ~1 m-thick tephra layer attributed to the RP eruption was found in the Lake Masoko sedimentary record around 25 km SSE of Rungwe (Garcin et al., 2006; Fontijn et al., 2012). More distal deposits are lacking and have likely undergone pedogenesis. However, sediment cores from Lake Malawi (SE of Rungwe) drilled up to 115 km from the summit showed visible ash horizons that can be chronologically correlated with the RP (Fontijn et al., 2011).

The spatial distribution of outcrops has been used to constrain the vent location to the current Rungwe summit though its precise crater location is unidentified. The outcrops are radially distributed around the summit and the near-circular shape of isopleths suggests that the eruption

occurred under wind-still conditions (Fontijn et al., 2011). An eruptive column of 30-35 km was inferred using the maximum lithics method (Carey and Sparks, 1986; Fontijn et al., 2011), which was likely sustained throughout the entire duration of the eruption, as no PDC deposits are found to be associated with the RP eruption. The peak mass discharge rate, calculated using a range of column heights, ranges from 2.8 to 4.8 $\times 10^8$ kg·s^{-1}, and the minimum erupted volume is estimated at 1.4 km^3 dense rock equivalent (Fontijn et al., 2011). This volume is reported as a probable underestimation by Fontjin et al (2011), as it does not include very proximal deposits (i.e., those deposited from the column margin) and especially lacks clear information on distal deposits. Given these parameters, the eruption was classified as Plinian yielding a VEI 5 (Newhall and Self, 1982; Fontijn et al., 2011).

A type section for RP was defined around 11.7 km SSE from the Rungwe summit and named KF176 in previous studies (Fontijn et al., 2010b, 2011, 2013). It consists of a ~2.5 m-thick, massive pumice deposit, that is reversely graded at the base and bounded by overlying and underlying palaeosols. The entire deposit was previously sampled by Fontijn et al. (2011) and divided into 14 subsamples every 20-25 cm from bottom to top and named from KF176-B to KF176-O, whereas KF176-A corresponds to the basal palaeosol.

Overall, the deposit grain-size distribution is unimodal and well-sorted (sorting $\sigma_\varphi < 2$) around the median at -2.2 φ (~4.5 mm) apart for the reversely graded base (lower 50 cm) which is finer (Fontijn et al., 2011). A similar trend is reflected by the total grain size distribution of the whole RP deposit, for which a median value is found around -2 φ (4 mm) using different interpolation models (Fontijn et al., 2011). Slight changes in whole rock compositions across the type section were observed by Fontjin et al. (2013), more precisely an increase of MgO, TiO_2 and CaO and a decrease of SiO_2 and MnO from bottom to top which led them to infer a possible chemical zonation of the magmatic reservoir. Storage conditions were estimated using the titanomagnetite-ilmenite pair geothermometer (Ghiorso and Evans, 2008) which yielded

temperatures in the 925-950 °C range and oxygen fugacity in the NNO+0.25-NNO+0.45 range (nickel-nickel oxide buffer; Fontijn et al., 2013). Reservoir ponding depths were estimated at 2.5-13 km in the shallow-mid crust with the clinopyroxene-liquid barometer (Putirka, 2008) and maximum pre-eruptive water content of 5.5 wt.% was estimated by difference from major element compositions of melt inclusions (Fontijn et al., 2013).

3 METHODS

3.1 Componentry analyses

The different types of clasts that constitute the coarse ash portion of the Runge Pumice deposit were investigated separately for each horizon of the type section (KF176-B to KF176-O). The 0.355-0.500 mm (1.5φ-1φ) and the 0.710-1.000 mm (0.5φ-0φ) grain-size ranges were selected for the observations (hereafter termed medium and coarse ash fraction respectively). The fractions were partitioned several times (up to 6) using a sample splitter to reduce the sample size and still maintain a representative and functional amount. With the aid of a stereomicroscope, the clasts were characterised and allocated to 3 classes, i.e. Juvenile, lithics and crystals (further subdivided into feldspars, mafic minerals, Fe-Ti oxides, haüyne and titanite), until a total of 3000 clasts per sample were categorised.

3.2 MI water content

To quantify the total amount of water dissolved within MI glasses we used the transmission Fourier Transformed Infrared spectroscopy technique (FTIR; §3.2.2). The FTIR method allows quantifying the sample absorbance for specific wavelengths in the near-/mid-infrared light range (usually between 1400 and 8000 cm^{-1}; von Aulock et al., 2014), which is caused by the vibration of specific molecules (analytes). The relationship between light absorption and the analyte concentration in the sample is described by the *Beer-Lambert Law,* which can be rewritten to express the analyte mass fraction (Stolper, 1982):

$$w = \frac{A \cdot M}{\epsilon \cdot l \cdot \rho} \times 100 \qquad (1)$$

where w is the analyte concentration in wt.%, A (dimensionless) the absorbance of the sample, corresponding to the height (or area) of specific peaks in the FTIR spectrum (§ 3.2.2), M the molecular weight of the analyte (e.g., 18.015 g·mol^{-1} for H_2O), ϵ (l·mol^{-1}·cm^{-1}) the composition-dependant absorptivity index of the sample for the analyte of interest, l (cm) the thickness of the sample crossed by the beam, and ρ the density of the sample (in g·l^{-1}).

3.2.1 Sample preparation

Alkali feldspar crystals in the RP deposit host MIs and embayments (i.e., inclusions open on one side), however, their lamellar shapes and tiny volumes made them impractical to be used for this study. MIs hosted in pyroxenes and Fe-Ti oxides were hard to identify due to the dark and opaque colour of the crystals. Haüyne crystals instead tend to contain visibly more MIs than the other mineral phases and therefore represented the best target for this investigation. Five stratigraphic horizons representative of the bottom (KF176-C), middle (KF176-G and KF176-K), and top (KF176-O) sequences of the deposit type section were selected. For each layer, several pumice clasts in the 11.3-16 mm (-3.5φ/-4φ) grain-size range were manually crushed. Over 100 haüyne crystals were handpicked from the crushed material in the 0.5-2 mm (1φ/-1φ) grain-size range and subjected to careful observation and sample selection. The crystals were placed on a glass slide and embedded in a thermosetting resin (Crystalbond™ 509). An exploratory first polishing of the crystal surfaces allowed a detailed description of MI features and recognition of potential melt inclusion assemblages (MIAs, i.e., groups of coeval MIs originated from the same magma at the same reservoir conditions; Bodnar and Student, 2006; Esposito et al., 2014) which helps in describing the history of both the MI and MI's host. Moreover, FTIR measurements require a clear path large enough to let the infrared beam pass through the sample to avoid any contamination of the spectrum. Therefore, small MIs (i.e.,

263 smaller than 15 μm, the minimum infrared beam aperture) or MIs hosting too many bubbles
264 were discarded (§ 4.2).

265 To ensure that only the MI was crossed by the infrared beam, the crystals hosting MIs or
266 embayments suitable for analyses were polished on two sides in a way that two parallel surfaces
267 of the selected MIs were exposed (doubly exposed; von Aulock et al., 2014). Firstly, the crystals
268 were grounded on one side with a 6 μm diamond paste until one or more MIs were properly
269 exposed. Final polishing was achieved with progressively finer-grade diamond pastes (3 μm
270 and 1 μm). Finally, the crystal was gently removed from the resin and flipped over to expose
271 and polish the opposite side of the MI following the same process. This way we obtained fragile
272 crystal wafers tens of micrometres thick. Eventually, a variable number of MIs per layer was
273 successfully prepared because of crystal availability and MIs' suitability for analyses, for a total
274 of 86 MIs and embayments.

275 *3.2.2 Infrared absorption*

276 The transmission FTIR spectra of MIs were acquired at the ISTO-CNRS laboratory (Orleans,
277 France) using a Nicolet 6700 FTIR spectrometer connected to a Nicolet Continuμm Infrared
278 Microscope equipped with a MCT IR Detector Module. The acquiring setup consisted of a
279 Globar light source, an XT-KBr beamsplitter and a 32x infinity-corrected Schwarzschild
280 objective matching to a 32x condenser. The crystals were gently removed from the resin after
281 heating on a hot plate, then rinsed in acetone to remove any resin residuals and placed over a
282 CaF_2 window.

283 The fundamental stretching vibration of O-H bonds in H_2O and OH^- absorbs infrared light at
284 the 3550 cm^{-1} wavenumber (**Fig. 2**). The height (or area) of this characteristic overtone peak in
285 IR spectra is directly proportional to the total concentration of water in the sample, and usually,
286 it retains a good signal-to-noise ratio. However, this overtone can be easily saturated at

relatively high water concentrations unless the thickness of the sample is extremely thin (von Aulock et al., 2014). In that case, water concentration can be measured by the combination of the absorbance band of the hydroxyl group (OH^-; 4500 cm^{-1}) with the band of molecular water (5200 cm^{-1}). Therefore, we acquired spectra in the 1200-6000 cm^{-1} wavenumbers unit range with a spectral resolution of 4 cm^{-1} (**Fig. 2**). The aperture of the square beam was set at 20x20 µm or 40x40 µm when the size of the MI allowed it, while a 15x15 µm beam aperture was exceptionally used for the smallest MIs. For each spectrum, 256 (512 for the 15x15 µm beam aperture) acquisitions were collected. A background spectrum on the CaF_2 window was collected for calibration before each sample analysis, and every time the spectra showed abnormal trends due to environmental changes in temperature, CO_2 concentration or humidity. We chose to use peak heights instead of areas as they are less subjected to peak distortions, especially for the combination bands. Finally, we adopted a linear baseline to measure peak intensity. A minimum of three scans were collected for each melt inclusion for reproducibility which were then averaged through the data processing tools of Omnic™ software to reduce the spectral noise. FTIR spectra were acquired at the centre of MIs but also closer to rims to evaluate the consistency of the estimated water content, while embayments were scanned in their most internal portions.

The molar absorptivity index in Eq. (1) is a composition-dependant constant that can be determined for each glass composition once the water content is constrained with other analytical methods (e.g., Karl Fisher titration or secondary ion mass spectrometry). However, absorptivity indices present in the literature for glasses with a chemical composition similar to that of the sample can be applied with good approximation (von Aulock et al., 2014). For high-alkali trachytic glasses a value of 66.9 ± 5.8 $l \cdot mol^{-1} \cdot cm^{-1}$ was experimentally determined for the 3550 cm^{-1} overtone (Behrens and Hahn, 2009) while absorptivity indices for the 4500 cm^{-1} and 5200 cm^{-1} overtones (ϵ_{4500} and ϵ_{5200}) were estimated through a multiple linear regression

based on the absorbance values of the 4500 cm^{-1} and 5200 cm^{-1} peaks (A_{4500} and A_{5200} respectively), according to the following relationship (Di Matteo et al., 2004):

$$\frac{w_{3550}}{100} = \frac{1}{\epsilon_{4500}} \cdot \frac{A_{4500} M}{l\rho} + \frac{1}{\epsilon_{5200}} \frac{A_{5200} M}{l\rho} \quad (2)$$

where w_{3550} is the water content (in wt.%) calculated with the 3550 cm^{-1} band and used as a fixed term for the regression. The regression was performed including those spectra that did not reach saturation and at the same time showed well-shaped combination bands. It was iteratively reproduced by systematically excluding those spectra values that deranged the interpolation until a satisfying goodness was achieved ($r^2 \approx 0.9$). The regressed molar absorptivity indices and their 90% confidence bounds (subscript and superscript values) measured $0.80^{1.51}_{0.09}$ $l \cdot mol^{-1} \cdot cm^{-1}$ and $1.97^{2.80}_{1.15}$ $l \cdot mol^{-1} \cdot cm^{-1}$ for the 4500 cm^{-1} and 5200 cm^{-1} overtones respectively. These indices are considerably different from those previously estimated for trachytic (1.58 $l \cdot mol^{-1} \cdot cm^{-1}$ and 1.36 $l \cdot mol^{-1} \cdot cm^{-1}$ respectively; Di Matteo et al., 2004) and phonolitic (1.25 $l \cdot mol^{-1} \cdot cm^{-1}$ and 1.10 $l \cdot mol^{-1} \cdot cm^{-1}$ respectively; Carroll and Blank, 1997) glass.

3.2.3 Thickness

The MI thickness is a fundamental parameter that must be carefully determined as it represents one of the major sources of error in Eq. (1), especially for the thinner crystal wafers. For example, in our dataset, a difference of 1 μm produces on average a ~3% percentage error on the water content estimation, equivalent to 0.1 wt.% H_2O. Moreover, during sample preparation, it is important to monitor the thickness of the samples as this could determine which absorbance band can be used (von Aulock et al., 2014). To minimise the uncertainty introduced by operator's biases (e.g., optical focus recognition) two different methods were applied, and the results compared. Firstly, the thickness was measured with a flat-anvil digital micrometer (resolution = 1 μm; accuracy = ±2 μm). A flat micrometer was chosen over a pointed micrometer to minimise the risk of damaging or disrupting the extremely fragile crystals. Once

we ensured that crystals were adhering properly to their glass slides, each glass slide was measured together with the hosted crystal and on its own. Crystal thickness was then obtained by difference. The measurements were repeated two or three times per crystal. Subsequently, we used an optical microscope with calibrated focus stages. A LEITZ DMR microscope equipped with an automated stage (resolution = 2 μm) was used, and each crystal was measured two times for consistency.

To verify the consistency of the thickness measurements, we applied the spectral fringes counting method for those transmission spectra that showed interference fringe patterns (Nichols and Wysoczanski, 2007; von Aulock et al., 2014). This method consists of counting the spectral fringes in a specific spectral region where no absorption peaks are present (usually in the 2000-2700 cm^{-1} range; Wysoczanski and Tani, 2006), and which relate to the thickness (l) following the equation (Nichols and Wysoczanski, 2007):

$$l = \frac{m}{2n(v_1 - v_2)} \qquad (3)$$

where m is the number of waves, n is the refractive index of the sample (dimensionless), and v_1 and v_2 are the highest and lowest wavenumber (in cm^{-1}) respectively of the selected spectral interval. Interference fringes were detected on both haüyne crystals and MIs, and refractive indices of 1.50 and 1.52 were used respectively (Taylor, 1967; Keller et al., 1978). While a good correlation was found between thicknesses measured with the optical focus stages method and the digital micrometer, a systematic underestimation (35.4% ± 18% percentage error on average) was observed between the results obtained with these methods and the thicknesses estimated by the interference fringes method. As the latter is considered less affected by operator biases and does not apply to all the MIs in the dataset because of interference recurrence, the measured thickness of each MI was increased by 35% to compensate for the underestimation.

358 *3.2.4 Glass density*

359 The density of MI glass has been estimated as a function of its chemical composition at room
360 temperature following the equation (Lange, 1997):

$$\rho_{298K} = \frac{\sum X_i M_i}{V_{298K}} \quad (4)$$

361 where X_i represents the mole fraction of each major oxide component (i), and M_i their molecular
362 weights. The volume of the glass at room temperature (V_{298K}) is considered equivalent to the
363 volume of the glass at the quenching temperature (V_{liq}) as no contraction after solidification is
364 expected because of the volume-constrained nature of MIs and the fast cooling in the
365 atmosphere of pumiceous tephra. Therefore, the contribution of the thermal expansion
366 coefficient (Eq. (4) in Lange, 1997) was not considered and the glass volume at quenching
367 temperature was estimated using the equation for iron-bearing silicate glasses, modified after
368 Lange and Carmichael (1987):

$$V_{liq}(T) = \sum X_i\,(T)V_i(T) + X_{Na_2O}X_{TiO_2}V_{Na_2O-TiO_2} + X_{H_2O}V_{H_2O}(T) \quad (5)$$

369 where V_i is the volume regression of major oxide components as a function of the liquid
370 temperature with respect to the volume at the modelled temperature of 1300 °C (Lange and
371 Carmichael, 1987):

$$V_i(T) = V_{i,1573K} + \frac{dV_i}{dT}(T - 1573K) \quad (6)$$

372 and $V_{H_2O}(T)$ is the temperature-dependent molar volume of water modelled starting from the
373 volume at ~1000 °C (Ochs III and Lange, 1999; Richet et al., 2000). The mole fractions of the
374 MI's major oxides (X_i) were derived from chemical analyses measured with a JEOL JX-
375 iHP200F field emission electron probe micro-analyser (EPMA) at the IMAP laboratories of the
376 Université Grenoble-Alpes (France). The crystal wafers were embedded in epoxy resin,
377 polished (down to 1 µm diamond grade), and carbon coated. We used an acceleration voltage

of 15 kV, a probe current of 5 nA, and a defocused beam diameter of 15 μm to analyse the MIs. The analytes were measured with four WDS (wavelength dispersive spectroscopy) and one EDS (energy dispersive spectroscopy; Si only, with StHs6-80 glass as calibration material) spectrometers. Sodium was analysed first to avoid element dispersion and a ZAF correction was applied. The StHs6-80, Atho-G and KE12 reference materials (Jochum et al., 2006) were analysed three times each, after every 30-40 measurements to evaluate accuracy. Each MI was measured at least three times for consistency. Water concentrations were roughly estimated from the difference of the sum of all the analytes from the equilibrated total concentration (100 wt.%; Devine et al., 1995).

To constrain the MI's quenching temperature *T,* equivalent to the fictive temperature of the pre-eruption silicate liquid, we applied the alkali feldspar-liquid geothermometer (Eq. (24b) in Putirka, 2008). This thermometer describes the chemical equilibrium between magmatic melts and alkali feldspars as a function of temperature. Alkali feldspar crystals were handpicked from the 0.5-2 mm grain-size fraction of crushed pumices and then embedded in epoxy resin. Pumiceous glass shards were obtained from the 125-250 μm grain-size fraction of manually crushed pumice clasts. The crushed material was rinsed and wet sieved at 80 μm in demineralised water to remove accretionary dust or clays and embedded in epoxy resin. Grain mounts of glass shards and alkali feldspar crystals were grounded and polished with diamond paste down to a grade of 1 μm. Alkali feldspar composition was analysed by EPMA, using the same instrument and analytical conditions as those used to analyse the haüyne-hosted MIs, and with Cr-Augite, Ortho-Bl3 and Ortho-Bl2 as secondary standards. For the glass shards, a 2 nA probe current and a 5 μm beam diameter were used. We analysed glass from each layer at least eight times for reproducibility, while core-to-rim transects of 5 measurements were performed on the alkali feldspars. As the alkali feldspar-liquid geothermometer does not foresee an equilibrium constant to constrain the equilibrium between melt and alkali feldspars (Putirka,

2008), we inspected the alkali feldspar crystals with backscattered electron imaging to evaluate the occurrence of resorption structures around the crystal rims. No signs of disequilibrium were identified. Imaging was performed in backscattered electron mode, with an accelerating voltage of 15 kV using a Hirox SH5500P scanning electronic microscope (SEM) equipped with a Bruker EDS Quantax detector at the Laboratoire G-Time of the Université libre de Bruxelles (Belgium).

The estimated hydrated glass density is 2.25 ± 0.01 $g \cdot cm^{-3}$ on average, a value slightly lower than densities generally accepted for trachytic and phonolitic glasses (Di Matteo et al., 2004). This discrepancy might be caused by the fact that we measured the density of the glass at the quenching temperature, corresponding to the liquid density, instead of room temperature.

3.3 Reservoir modelling

To constrain the pre-eruptive conditions of the magmatic reservoir, we applied different petrological models well established in the literature. To our knowledge, haüyne-melt equilibrium-based geothermometers have not been experimentally described. Therefore, haüyne-hosted MIs were equilibrated with alkali feldspars, the most recurrent crystal throughout the deposit, and the most stable mineralogical phase during the entire crystallisation sequence. For each sample, the entrapment temperature was estimated by comparing the K-feldspar-liquid hygrometer developed by Mollo et al. (2015) and the alkali feldspar-liquid geothermometer from Putirka (calibration error ±23 °C; Putirka, 2008). The K-feldspar-liquid hygrometer was inverted to express temperature as a function of the water concentrations computed through FTIR analyses. Each MI glass composition was equilibrated with the core, middle and rim portions of each alkali feldspar collected from its corresponding deposit horizon, allowing to obtain a predicted equilibrium constant (Kd; Eq. (2) in Mollo et al., 2015). The best correlation between the resulting Kd and the measured equilibrium constant

(Supplementary Material in Mollo et al., 2015) was found between MIs and the rim of alkali feldspars. Therefore, entrapment temperatures were estimated by pairing each MI with the rim of each crystal from the corresponding horizon, and the results were averaged to express variance. Additionally, the occurrence of possible chemical zonation in alkali feldspars was investigated with SEM imaging and chemical mapping. Once temperature and water content are constrained, the minimum pressure in the magmatic reservoir at the moment of MI entrapment was computed through the MagmaSat (Ghiorso and Gualda, 2015), MooreWater (Moore et al., 1998), Iacono-MarzianoWater (Iacono-Marziano et al., 2012), and ShishkinaWater (Shishkina et al., 2014) water solubility models, all available within the VESIcal python3 library (v. 1.2.6.; Iacovino et al., 2021).

The same procedure used to measure the water concentration in MIs through FTIR analysis was then applied to estimate the H_2O and CO_2 content in MI-hosting haüyne crystals. Spectra were acquired close to the MIs adopting the same acquisition settings and a beam aperture of 40x40 µm. As the haüyne absorbance spectrum for water is composed of three overlapping overtones in the ~2800 – 3700 cm^{-1} range, the integrated absorbance was used (Bellatreccia et al., 2009), while the stretching of structural CO_2 molecules gives a well-defined absorbance peak at ~2350 cm^{-1} (**Fig. 2**). The composition-dependant integrated molar absorptivity indexes for H_2O and CO_2 were fixed at 5422 $l \cdot mol^{-1} \cdot cm^{-2}$ and 1866 $l \cdot mol^{-1} \cdot cm^{-2}$ respectively for haüyne of similar compositions (Bellatreccia et al., 2009), while the crystal density was estimated to be 2.4 $g \cdot cm^{-3}$ (Taylor, 1967).

A principal component analysis of MI major element concentrations allowed to identify the most relevant oxides affecting the chemical variability of the magma, in an attempt to identify chemically differentiated magmas co-occurring in the magmatic reservoir. The three most representative principal components were used to identify chemically distinct clusters of MIs through hierarchical clustering. The crystallisation history of the magma was characterised by

modelling the liquid line of descent of magmatic compositions starting from the composition of a possible Rungwe mafic parental magma (**Table 1**; Furman, 1995). The rhyolite-MELTS (v. 1.0.2.; Gualda et al., 2012a; Ghiorso and Gualda, 2015) source code was used for the modelling, imposing a fractional crystallisation of olivine, clinopyroxene, orthopyroxene, hornblende, biotite, plagioclase, alkali feldspar, nepheline, kalsilite, leucite, spinel, apatite and rutile, and an oxygen fugacity fixed at the FMQ +1 buffer (~+0.42 NNO; Fontijn et al., 2013). The final temperature was set to the average quenching temperature estimated from the application of the alkali feldspar-liquid geothermometer (§3.2.4), whereas pressure was changed iteratively in the range given by the lowest pressure estimated from MI calculations (~650 bar; §4.4.1) and the pressure at 10 km depth (~2700 bar), considered an acceptable depth for deep crystalline mush accumulation (Huber et al., 2019). The available chemical analyses of the potential mafic parental magma (Furman, 1995) do not contain water concentrations. However, to fit the amount of water we measured in the final magma, we assumed the initial mafic magma to contain between 0 and 1.1 wt.% of water, a range commonly accepted for rift basalts (White et al., 2012; Rowe et al., 2015; Hutchison et al., 2018). Magma compositions were re-normalised with this presumed water content.

Whole-rock major and trace element concentrations were determined for pumices of each deposit horizon (KF176-B to KF176-O) at the Laboratoire G-Time of the Université libre de Bruxelles (Belgium). Samples were manually crushed to powders in an agate mortar and then prepared as a solution by alkaline fusion. Loss on ignition (LOI) was estimated by heating the powders at 800 °C for 2h after having dried them completely at 105 °C for over 24h. Major elements were measured with a Thermo Fisher Scientific iCAP inductively coupled plasma-optical emission spectrometer (ICP-OES) using Y as an internal standard. Trace elements were measured with an Agilent 7700 quadrupole inductive-coupled plasma mass spectrometry (Q-ICP-MS) operated with a He-filled collision cell. The USGS standards BHVO-2, RGM-2, and

QLO-2 were analysed as reference materials and one sample was measured twice for reproducibility. The total reproducibility based on reference materials was estimated to be better than 4% and 12% relative standard deviation for major and trace elements respectively.

4 RESULTS

4.1 Componentry analyses

The coarse ash fraction of the deposit analysed is composed of three broad clast types: i) juvenile, ii) lithics, and iii) crystals. Juvenile clasts are cream-white highly vesicular pumices. Clast shapes are mostly solid, equidimensional and subrounded but, according to the size and shape of vesicles, can be more elongated or irregular. Lithic clasts include rock fragments of different nature extracted from the volcanic edifice, older lava deposits, and holocrystalline rocks. Free crystal phases include alkali feldspar, haüyne, pyroxene, biotite, Fe-Ti oxides, titanite, and accessory olivine. In the coarser ash fraction, the juvenile class is dominant in each layer of the deposit (always > 65% of the components), but it is substantially less dominant in the medium ash fraction (between 45% and 80% of the components) where the crystal content reaches up to the 45% of the components (**Fig. 3**). A gradual increase of the crystal content is observed from the bottom to the top of the stratigraphic section, particularly for the medium ash fraction, associated with an opposite trend of the juvenile content (**Fig. 3**). The lithic component represents a small fraction of both analysed grain sizes (3 - 12%) and it is almost constant along the stratigraphic section, except for a peak around 25 cm from the bottom (samples KF176C-KF176D) where it reaches up to 28% of the components (**Fig. 3**).

On average, 88% ± 3% and 96% ± 2% of the crystal component within the medium and coarse ash fractions respectively are represented by alkali feldspars (**Fig. 3**). Mafic minerals (pyroxenes and biotite) are the second most abundant crystalline component (between 3.4% and 10.5%) followed by Fe-Ti oxides (between 1.5% and 9.0%). Relative crystal abundances

are almost constant throughout the stratigraphic column, apart from haüyne which shows a progressive increase from bottom to top, even though it never represents more than 3% of the crystal population (**Fig. 3**). The medium ash contains a smaller amount of haüyne, which is absent in the bottom 150 cm of the deposit (**Fig. 3**). Titanite crystals are found only in the medium ash and in small numbers (always < 0.9%).

4.2 Melt inclusion textures

MIs and embayments are ubiquitous features of haüyne crystals of the RP deposit. A comprehensive description of the MIs is provided in the **Supplementary Table 1**.

The colour of MIs ranges from pale to dark brown and is related to MI thickness and bubble content. The volume of MIs varies by about six orders of magnitude (10^3-10^8 μm^3; equivalent ellipsoid volume) but their sizes are relatively large (major axis 147 ± 122 μm on average) and altogether they can occupy a considerable part of the crystals. All MIs tend to have blunt morphologies, but the vast majority are ellipsoidal or sub-spherical (ca. 44% and 23% respectively; **Fig. 4a**). Funnel-like MIs and embayments can be found in pairs often coaxial and connected by a tapered bottleneck (**Fig. 4b, c**). The distribution of MIs within the crystals appears to be arbitrary and does not create evident textural zonation. Only elongated MIs tend to have the major axis oriented sub-parallel to one crystallographic face, an arrangement particularly evident for MIs which mirror crystal growth stages with clusters of sub-parallel, planar MIs (**Fig. 4d**). Despite some inclusions having near-angular morphologies, fully faceted MIs are extremely rare (ca. 2%). Within the same crystal, it is common to find MIs of different shapes or sizes, and no correlation exists with the height in the stratigraphic section. Most embayments show irregular morphologies that cannot be geometrically described (termed *complex* as in Ruefer et al., 2021). Subsequently, sub-cylindrical (simple) and bulbous morphologies are the second most represented.

Other than one MI hosting a micrometric apatite crystal, crystalline phases are absent in MIs while the number and size of bubbles were the most distinctive features in separating MIs that experienced similar entrapping histories. The MIs observed can be free of bubbles (**Fig. 4a**), host a single, spherical, shrinkage bubble (**Fig. 4a**), or be partially (or entirely) filled with a multitude of microscopic bubbles (termed microvesicular MIs; **Fig. 4c, f**). On rare occasions, MIs host several bubbles (usually less than 10) of variable size (**Fig. 4e**). Bubble-free MIs are overall the most abundant, especially in the lowest stratigraphic horizon, followed by single-bubble MIs and microvesicular MIs, whereas the latter are particularly present in top horizon O (**Fig. 4g**). The size of shrinkage bubbles varies between different MIs but scales well with their size. The bubble volume in single-bubble MIs occupies on average 2.21 ± 1.62% of the inclusion volume, whereas in a microscopic bubble it covers at most 0.23 vol.% (0.04 ± 0.06 vol.% on average; **Fig. 4h**), and the bubble size can reach up to 41.7 μm and 5.1 μm in diameter respectively. We acknowledge that a large standard deviation results from the assumption of the equivalent ellipsoidal volume as the MI volume. Bubbles occurring in couples or groups of a maximum of ten bubbles, generally include one larger bubble, whose volume occupancy is comparable to that of the single bubbles, and several smaller bubbles whose occupancy can be as small as that of microscopic bubbles. No evident correlation is shown between the number and size of bubbles and the size and geometry of MIs. Noteworthy, groups of MIs hosted in the same crystal generally contain the same amount of bubbles that share a similar volume occupancy. Only bubble-free and single-bubble inclusions which do not show any post-entrapment modification (e.g., leaking through fractures) were considered for further analyses. Embayments often host a multitude of discrete large bubbles (10.77 ± 0.78 vol.% on average) that concentrate, and seem to propagate, from the outlet where they assume ellipsoidal to droplet shapes (**Fig. 4f**). If bubbles do not fully form inside the embayments, these might be present at the outlet as a large bubble variably intruding from the glass attached to the crystal exterior.

These characteristic bubble assemblages facilitate the recognition of embayments when the outlet is hidden.

4.3 MI's water content

Water concentration in MIs ranges from 1.89 wt.% to 5.59 wt.%, with an average of 2.85 ± 0.8 wt.%. Embayments contain slightly less water, showing an average of 2.16 ± 0.46 wt.%, while no noticeable variation is detected between MIs that have or do not have a vapour bubble (2.81 ± 0.55 wt.% and 2.89 ± 0.96 wt.% on average respectively). Similar water contents are observed in MIs and embayments collected from different horizons within the deposit, however on average MIs in layer C contain less water (i.e., 2.40 ± 0.67 wt.%; **Fig. 5a**), while a mild, progressive decrease can be observed in embayments from horizon C to O. Water concentrations given by the combination of the 4500 cm^{-1} and 5200 cm^{-1} overtones were consistent with concentrations estimated using the 3500 cm^{-1} overtone (**Fig. 5b**). On average, a percentage difference of 17 ± 16% between the two approaches was observed. However, water concentrations given by the combination of the 4500 cm^{-1} and 5200 cm^{-1} overtones were considered only in the rare case when the 3500 cm^{-1} overtone reached saturation. The uncertainty given by the error propagation of every parameter in Eq. (1) is on average 12 ± 4%, which is comparable to the uncertainty generally expected from this type of estimation (e.g., 10-20%; Agrinier and Jendrzejewski, 2000; Wysoczanski and Tani, 2006; von Aulock et al., 2014).

4.4 Reservoir modelling

4.4.1 Geothermobarometry

Entrapment temperatures estimated for MIs with the K-feldspar-liquid hygrometer range between ~830 and 1275 °C, with an average at ~1110 ± 96 °C (**Fig. 6a**). Embayments record a similar, but slightly higher, range of temperatures, with an average at ~1203 ± 66 °C. No

substantial temperature variations are shown by MIs of different stratigraphic horizons (**Fig. 6a**). Temperatures estimated with the Putirka (2008) alkali feldspar-liquid geothermometer resulted on average in a lower but tighter temperature range: from ~ 938 to 1054 °C for MIs and from ~ 942 to 1011 °C for embayments. Overall, temperatures estimated with the Putirka (2008) geothermometer are comparable but slightly higher than values previously estimated from Fe-Ti oxide pairs (i.e., 915-950 °C; Fontijn et al., 2013).

Minimum lithostatic pressures given by the different solubility models are consistent, apart from the Iacono-MarzianoWater model which significantly deviates from the other models (**Fig. 6b**) and are not visibly affected by the temperature estimation method used Statistical values for each solubility model are reported in **Supplementary Table 2**. Pressures range between 30 and 194 MPa, lower than previously estimated from the clinopyroxene-liquid barometer (i.e., 70-350 MPa; Fontijn et al., 2013). We emphasise that the pressures estimated refer to the minimum entrapping pressure as, for a given melt temperature and composition, the solubility models compute the pressure at saturation, for which we however do not observe any petrographic evidence. Pressures recorded from different horizons do not indicate substantial differences, except for horizon G which gives a more scattered distribution due to outlier values (**Fig. 6b**). Embayments result on average in slightly lower, but more clustered, pressure values.

4.4.2 Glass geochemistry

Melt inclusions have a homogeneous trachytic-phonolitic composition, with around ~61 ± 0.3 wt.% SiO_2 and an elevated alkaline elements content (**Fig. 7**). The agpaitic index ([Na+K]/[Al]) ranges between 0.99 and 1.07 with an average at 1.02 ± 0.02 while the Mg# ([Mg]/[Mg+Fe]) is 0.22 ± 0.01 on average. The full range of chemical compositions is provided in the **Supplementary Table 3**. Comparisons of different element concentrations do not show any evident trend apart from the positive correlation of CaO and MgO concentrations and the

598 negative correlation of Na_2O and K_2O (**Fig. 8a, b**). Embayments and MIs have similar major
599 element concentrations, only K_2O tends to be slightly higher in MIs. Overall, the glass
600 composition within a single MI or embayment is chemically homogenous and does not show
601 any systematic variation from core to rims (e.g., relative standard deviation equals 0.36 ± 0.20%
602 and 1.34 ± 1.09% on average for SiO_2 and Na_2O respectively), even for more mobile elements
603 as Cl and S in open embayments. Major element concentrations in MIs are roughly constant
604 through the different horizons (i.e., relative standard deviation between 0.16% in FeO and
605 9.42% in P_2O_5), however, a slight increase of K_2O and TiO_2, and a decrease of Na_2O occur from
606 layer C to layer O (**Fig. 8c**). The chemical composition of pumice matrix glass is overall similar
607 to that of the MIs and embayments for silica and most of the major elements (**Fig. 7**) but is
608 slightly depleted in K_2O (-7.0 ± 1.0% on average) and enriched in Na_2O (+9.4 ± 4.4% on
609 average). Tephra glass shows a more systematic variation of element/oxide concentrations from
610 base to top of the stratigraphic succession. Particularly, K_2O, MgO, TiO_2, SO_3, and CaO
611 concentrations tend to decrease, whereas Na_2O and Cl increase towards the top (**Table 1; Fig.**
612 **8c**).

613 The principal component analysis of MI glass composition suggests that the chemical variance
614 is dominated by K_2O, Na_2O and SiO_2, which constitute the majority of the first three principal
615 components and represent a total variance of ~26%, ~25% and ~23% respectively. The attempt
616 to cluster the MIs according to their stratigraphic horizon was unsuccessful. Instead, the first
617 three principal components, which represent ~96% of the variance, were used to group the data
618 into two major chemical clusters plus an outlier sample (**Fig. 9**) through a hierarchical
619 clustering. While the first cluster includes only six MIs, the second cluster includes most of the
620 MI dataset and represents a slightly more silicic magma, enriched in Na_2O and depleted in K_2O
621 (**Fig. 9**). The incorporation of MIs in one or the other cluster is not related to the distribution
622 within crystals or to whether it hosts a shrinkage bubble. However, all the MIs belonging to the

more evolved first cluster are found in the topmost stratigraphic horizons. Additionally, the temperatures estimated from the first cluster are on average slightly higher, while pressure estimations largely overlap.

Multiple tests were performed in Rhyolite-MELTS to identify a possible liquid line of descent that might match the crystallisation path that generated the chemical composition of the erupted magma. However, the lack of intermediate compositions did not allow us to verify the occurrence of multi-step crystallisation. The best match was obtained for K_2O, TiO_2, SiO_2, CaO and MgO adding 0.3 wt.% of water to the initial mafic composition before normalisation (**Fig. 10**). For the range of pressures considered, the liquid line of descent corresponds to ~85% fractional crystallisation of the parental magma, which is dominated in the initial stages by olivine and clinopyroxene until alkali feldspar starts to form. Some phases fractionated from the magma (e.g., spinel) as suggested by the model are not identified in the deposit. These phases might be early forming crystals that were fractionated in the magmatic mush at depth. Haüyne, or any other phases of the sodalite group, cannot be included as a fractionating solid in the model, therefore the modelled crystallisation of another feldspathoid mineral such as leucite (not observed in the deposit) might partially explain the enrichment in Na and Ca in the modelled composition compared to the measured values.

The bulk composition of pumice is similar in major elements to the matrix glass, though slightly depleted in SiO_2 (-3.6 ± 0.9 wt.% on average) and Na_2O (-2.3 ± 0.5 wt.% on average), while the amount of Al_2O_3 is higher (+1.6 ± 0.5 on average). Across the stratigraphic section, the composition progressively decreases in SiO_2 and becomes enriched in TiO_2, CaO, MgO, P_2O_5 from bottom to top. The other oxides remain stable. Noteworthy, the composition of the bottom horizon B differs considerably from the other horizons, showing anomalous trends in Al_2O_3, FeO_{tot}, MnO, K_2O and TiO_2. Trace element concentrations of bulk pumices are reported in **Table 1**. The primitive mantle-normalised (McDonough and Sun, 1995) concentrations are

overall higher than values previously recorded in Rungwe basalts (Castillo et al., 2014), but they show similar trends (**Fig. 11a**). The highest normalised values are observed for highly incompatible U and Th. REE concentrations normalised to the primitive mantle (McDonough and Sun, 1995) indicate higher concentrations of LREE compared to HREE and a marked negative Eu anomaly (**Fig. 11b**). Progressive increasing or decreasing trends are observed across the stratigraphy (**Fig. 11c**). Particularly, from bottom to top, most of the middle REE and LILE (apart from Rb) tend to increase, while extreme HREE or LREE and HFSE show an opposite trend. Substituent metals of Fe-Mg do not show any particular trend. Noteworthy, for several elements, the bottom horizon (i.e., sample KF176_B) retains anomalous values (**Fig. 11c**).

4.4.3 Crystal geochemistry

The composition of alkali feldspars is homogeneous and ranges from $Ab_{71}Or_{28}An_{1}$ to $Ab_{54}Or_{44}An_{2}$ (**Supplementary Fig. 1a**; **Supplementary Table 3**). Textural observations did not indicate any visible chemical zonation of the crystals (**Supplementary Fig. 1a,b**). Across the stratigraphic section, the anorthite component tends to increase from bottom to top, which correlates to a progressive increase of CaO at the expense of Na_2O, while K_2O remains essentially stable.

Haüyne is also chemically homogenous and did not show any visible chemical zonation. Haüyne crystals from different horizons have similar chemical compositions (**Supplementary Table 3**), apart from a subtle, progressive, increase of SO_3 (wt.%) from the bottom to the top of the deposit. Water content within the crystals estimated with FTIR analyses ranges from 0.49 wt.% to 2.16 wt.% with an average at 1.14 ± 0.37 wt.% and tends to decrease across the stratigraphic section, whereas CO_2 ranges from 0.39 wt.% to 2.06 wt.% and tends to remain quite homogeneous. The stoichiometric formulae of the haüyne crystals can be written as:

$$(Na_{5.44-6.15}Ca_{1.61-1.87}K_{0.2-0.26}Fe_{0.04-0.05}Mg_{0.01-0.03})_{\sum\cong 8}(Al_{5.78-5.86}Si_{6.14-6.22}O_{24}) \cdot [(SO_4^{2-})_{1.37-1.73}(CO_3^{2-})_{0.10-0.46}(Cl^-)_{0.07-0.14}(OH^-)_{0.00-0.19}]_{\sum=2} \cdot nH_2O \quad (7)$$

where *n* ranges from 0.68 to 2.68. The unit formula was normalised considering (Si + Al) = 12, while the anionic site equals 2 for the purpose of the occupancy of water. As the overtone at ~3500 cm^{-1} used to estimate water content from FTIR spectra does not resolve the speciation of water, we allocated water to the OH^- group in the anionic site to complete a valence of 2 (Bellatreccia et al., 2009), and the remaining water was added as molecular water. All the sulphur was allocated to sulphate (SO_4^{2-}) as haüyne is known to be stable at more oxidising conditions (Baudouin and Parat, 2015 and references therein) and because of the presence of sharp overtones at ~2200 cm^{-1} in FTIR spectra (Bellatreccia et al., 2009). The ubiquitous occurrence of Ca in the stoichiometric formulae (Eq. 7) confirms that all the crystals analysed are close to the haüyne end-member in the haüyne-nosean solid solution. However, a progressive increase of Ca and SO_4, and an opposite decrease of Na are observed across the stratigraphic unit from horizon C to horizon O, implying subtle variations in the haüyne-nosean series. Apart from melt inclusions, haüyne crystals host biotite, ilmenite and apatite crystals. The crystal edges are commonly altered to unidentified zeolitic phases, which are enriched in Si and Al and banded with Ca enrichments (**Supplementary Figure 2**).

5 DISCUSSION

The type section for the Rungwe Pumice fall deposit (outcrop KF176) discussed in this study consists of a massive, 250 cm-thick pumice fall deposit which was previously sampled every ca. 15-20 cm (Fontijn et al., 2010b, 2011). To interpret the geochemical data, we considered samples collected at the base of the stratigraphic section (e.g., KF176_B), representative of the topmost portions of the magmatic reservoir at the moment of the eruption, while, in contrast, the top deposit horizons (e.g., KF176_O) represent the deepest part of the plumbing system that

694 fed the eruption. Pumice clasts forming the finer-graded horizon KF176_B are slightly darker
695 and softer than pumices of the overlying deposit horizons, appearing visibly more altered.
696 Reverse grading at the base of RP deposits was identified only at outcrops located SE of
697 Rungwe and close to the vent, where also isopach tends to be slightly thicker (Fontijn et al.,
698 2010b). This might suggest an initial opening phase of lower explosivity emplacing a fine-
699 grained lapilli fallout deposit mostly in the south, followed by a temporal hiatus long enough
700 to allow early alteration processes to act on the pumice glass. Subsequently, the peak in lithics
701 in KF176_C may correlate with a conduit-clearing event during the initial stages of the eruption,
702 which is also consistent with the reverse grading at the base (Fontijn et al., 2011). Additionally,
703 the progressive increase of crystal components toward the top portions of the deposit suggests
704 the accumulation of crystals in the deeper parts of the magmatic reservoir (**Fig. 3**), which is
705 particularly accentuated in the medium ash fraction.

706 **5.1 Melt Inclusions**

707 Different types of information about the conditions of magma accumulation at depth can be
708 inferred from petrographic, geochemical, and modelling investigations of crystal-hosted melt
709 inclusions (Danyushevsky et al., 2002; Rose-Koga et al., 2021). Such relevant data can then be
710 used to describe the pre-eruptive processes that eventually lead to magma ascent, fragmentation,
711 and eruption. At the same time, care is needed before interpretation as entrapment conditions
712 or post-entrapment modifications can alter the properties of a MI (Esposito et al., 2014;
713 Cannatelli et al., 2016).

714 *5.1.1 Morphology*

715 Melt inclusions entrapped in RP's haüyne crystals have discrete morphologies and variable
716 sizes. Their distribution within crystals does not exhibit any textural pattern that implies
717 variations in crystal growth rate induced by magmatic recharge (Cooper et al., 2015), but their

718 ubiquitous presence in haüynes, from cores to rims, might imply a steady crystal growth.
719 Additionally, their erratic allocation within crystals, unrelated to phenocryst growth zones,
720 made the recognition of separated melt inclusion assemblages (MIAs; Bodnar and Student,
721 2006) impractical. The assumption that specific groups of MIs may have formed at the same
722 reservoir conditions was therefore unattainable from petrographic observations (Esposito et al.,
723 2014).

724 Specific morphologies such as funnel-shaped MIs and embayments (termed *curvilinear*; Faure
725 and Schiano, 2005), were observed in olivine during single-stage, low-rate, cooling
726 experiments, and associated with the growth of crystals at equilibrium (Faure and Schiano,
727 2005). The common occurrence of similar morphologies in haüyne suggests that even the most
728 irregular MIs can be formed at a constant, low undercooling, crystal growth in the absence of
729 dissolution by local disequilibrium induced by fluid bubbles. Embayments might be the result
730 of incomplete inclusion entrapment.

731 Haüyne-hosted MIs in our dataset have blunt/subrounded shapes while fully faceted
732 morphologies are rare (< 2%). For quartz-hosted MIs and embayments, the diffusion-dependent
733 faceting process has been inferred to occur in tens to hundreds of years according to the
734 inclusion size (Gualda et al., 2012b; Pamukcu et al., 2015; Ruefer et al., 2021) and assuming
735 that post-entrapment crystallisation is hindered. The relationship between MI size and faceting
736 times described in Gualda et al. (2012b) for quartz hosts cannot be applied directly to haüyne,
737 as diffusion for elements other than silica must be considered. Additionally, we note that this
738 geospeedometer is temperature-dependent and tested with substantially lower temperatures in
739 Gualda et al. (2012b). Higher temperatures might delay faceting resulting in longer crystal
740 residence times. However, the occurrence of sub-rounded MIs as small as 15 μm in diameter at
741 the core of crystals suggests that haüyne growth and inclusion entrapment occurred shortly on

742 geological timescales (tens to hundreds of years) before the eruption, which is also supported
743 by the absence of microlites or growth rims within the MIs.

744 Further implications on entrapping conditions and crystallisation history are given by the
745 amount and size of bubbles in MIs. Vapour bubbles found within MIs might be entrapped during
746 MI formation if a separate vapour phase was present in the magma (i.e., in case of volatile
747 saturation) or formed within the MI (Davidson and Kamenetsky, 2007). A single post-
748 entrapment bubble can form due to volatile oversaturation induced by post-entrapment
749 crystallisation or due to different degrees of contraction exerted by the melt compared to the
750 host crystal (Danyushevsky et al., 2002; Cannatelli et al., 2016; Rose-Koga et al., 2021 and
751 reference therein). The volume percentage occupied by single bubbles in haüyne-hosted MIs is
752 small and overall constant when comparing inclusions hosted in the same crystal, crystals
753 located in the same horizon, and even across the stratigraphic section. This implies that the
754 bubbles formed within the MIs in the absence of pre-entrapment vapour phases (Danyushevsky
755 et al., 2002; Moore et al., 2015; Cannatelli et al., 2016; Rose-Koga et al., 2021). Additionally,
756 based on petrographic and geochemical observations (see hereafter) we exclude that a post-
757 entrapment crystallisation might have occurred, therefore the formation of a single bubble is
758 interpreted as caused by the shrinking of the melt during cooling (Cannatelli et al., 2016; Rose-
759 Koga et al., 2021 and references therein). If instead, the cooling rate is excessively fast, the
760 bubble does not have enough time to nucleate before quenching and the MI results free of
761 bubbles (Cannatelli et al., 2016). The bubble-free type of MIs is overall the most abundant,
762 particularly in crystals located at the shallower levels of the magmatic reservoir prior to the
763 eruption, suggesting elevated ascent and cooling rates. Single bubbles instead formed mostly
764 in crystals coming from the lower portions of the magmatic reservoir, where they might have
765 had more time to cool during the eruption. Textures like those of microvesicular MIs have been
766 observed in re-homogenisation experiments of volatile-saturated MI entrapping a primary

767 vapour bubble (Esposito et al., 2012). Therefore, we infer these MIs were likely entrapped in
768 volatile-saturated portions of the magmatic reservoir. Additionally, they host microscopic
769 bubbles that can occupy the entire MI but also much larger bubbles, suggesting a volatile phase
770 was already separated from the melt during entrapment and not formed inside the inclusion
771 (Cannatelli et al., 2016; Steele-MacInnis et al., 2017). Decrepitation and leaking processes, or
772 alternatively differential shrinking at high quenching rates, are instead inferred to cause
773 inclusions hosting several bubbles of different sizes (Cannatelli et al., 2016). As we are not able
774 to discern their formation process, we considered those MIs unsuitable for this study and they
775 were not investigated further. The formation of large, tapered, bubbles propagating from
776 embayment outlets is instead associated with syn-eruptive melt supersaturation that led to
777 volatile degassing and vesiculation just before quenching (Ruefer et al., 2021). Bubbles are
778 present within embayments either intruding from the outlet or forming discrete bubbles,
779 however, experimental observations proved that different bubble textures can be generated by
780 the same decompression history (Hosseini et al., 2023). The reason why bubbles concentrate at
781 the outlet of embayments can be explained by the fact that melt inside the embayment does not
782 react to decompression disequilibrium in the same way as the melt outside. Therefore, bubbles
783 tend to form in portions of embayments closer to the free melt and likely migrate in and out of
784 the embayment. Preservation of supersaturated conditions in embayments and MIs also inhibits
785 decompression-induced microlite formation (Ruefer et al., 2021) as shown by the total absence
786 of microlites within the embayments studied.

787 *5.1.2 Melt composition*

788 When dealing with the chemical composition of MIs it is fundamental to assess the
789 representativity of the original melt. We exclude that post-entrapment crystallisation (Esposito
790 et al., 2011, 2014) occurred to modify the chemical composition of MIs in our dataset. Glass is
791 homogeneous within each MI and no zonation is observed within the host around them.

Additionally, given the similarity of MI compositions with those of tephra glass and the independence from MI size, we also exclude a boundary layer effect that would have caused the inclusion to entrap a non-representative portion of melt (Faure and Schiano, 2005; Esposito et al., 2014). Furthermore, experimental studies indicated that well-shaped, euhedral crystals growing at lower cooling rates tend to collect a representative portion of parental melt in contrast to diffusion-governed, fast-growing, skeletal/dendritic crystals (Faure and Schiano, 2005).

From chemical modelling of the potential liquid line of descent, we infer that the RP phonolitic/tephritic composition can be derived by over 80% fractional crystallisation of a basaltic parental magma. However, we emphasise that there is no concrete evidence that these early basaltic products of Rungwe are cogenetic to RP magma. Moreover, there is no consensus about processes that can originate phonolitic and peralkaline trachytic magmas. Several studies suggest that these might not be generated solely by fractional crystallisation but invoke a contribution of direct mantle partial melting or volatile-induced crustal assimilation (Macdonald, 1987; Scaillet and MacDonald, 2001; Baudouin and Parat, 2015 and references therein). More targeted investigations are required.

Major element concentrations within haüyne-hosted MIs of RP are overall constant throughout the different deposit's horizons suggesting the entrapment of a chemically homogeneous magma. Even the clustering of principal components does not reveal substantial chemical differentiation apart from a subtle increase of magmatic evolution from the bottom of the reservoir, which is inferred by the preferential occurrence of MIs from the slightly less evolved cluster at the topmost horizons K and O in the stratigraphic section. In any case, embayment chemical compositions overlap those of MIs, inferring that once haüyne started to crystallise the magma did not undergo excessive compositional evolution. The major element composition of MIs is also substantially closer to that of the pumice matrix glass compared to pre-

817 differentiation bulk rock compositions (**Fig. 12**), inferring that MIs most likely sampled the
818 very last and most evolved magma before the eruption. Comparison with chemical
819 concentrations of MIs entrapped in mafic hosts showed less evolved compositions (**Fig. 12**;
820 Fontijn et al., 2013), implying that differentiation processes occurred before haüyne started to
821 form. This is confirmed by trace element concentrations of pumice whole rock indicating a
822 certain degree of differentiation within the magmatic reservoir. The progressive enrichment of
823 the most compatible trace elements with depth in the magmatic reservoir infers an advanced
824 degree of fractional crystallisation in its shallowest portions where the compatible elements
825 (e.g., mostly Ba, Sr, and Eu compatible in alkali feldspars) are caught during crystallisation and,
826 in contrast, incompatible elements are enriched in the residual melt. Considering the extreme
827 case of maximum incompatibility (i.e., bulk partition coefficient $D = 0$) for those elements that
828 showed the higher enrichment with height in the stratigraphic section (i.e., U and Th), we
829 observed that the trend between horizon KF176_B and KF176_O corresponds to a minimum
830 of 60% Rayleigh fractional crystallisation, meaning the whole rock of horizon KF176_B
831 corresponds to the 40% residual melt of the magma in horizon KF176_O (**Fig. 11d**).

832 A similar result is obtained by comparing the trends of compatible against incompatible trace
833 elements for a range of pumice bulk partition coefficients (**Fig. 11c**). Only the horizon KF176_B
834 diverts strongly from the general trend, having much higher values of Ba (and other compatible
835 elements such as Sr) than expected. While lower SiO_2 and total alkali and higher FeO_{tot} and
836 compatible trace element concentrations of KF176_B whole-rock composition may suggest a
837 less evolved magma, its depletion in MgO and enrichment in incompatible elements compared
838 to the rest of the deposit implies a more advanced stage of evolution. This early-extracted
839 magma may therefore represent an older and separate, shallow mush zone of the reservoir where
840 fractionation of crystals was less efficient and instead an *in-situ* equilibrium crystallisation was
841 promoted. This may explain a lower fractionation of compatible elements as observed at the

topmost regions of crystalline intrusions (Namur and Humphreys, 2018). Discarding horizon KF176_B from the main trend suggests a lower degree of fractional crystallisation (**Fig. 11c, d**). Nonetheless, the crystal-poorer topmost portions of the magmatic chamber yield the highest degree of crystallisation, consistent with an effective fractionation of crystals that are physically separated toward the reservoir walls or sink in the crystal-richer reservoir bottom (e.g., horizon KF176_O), and also suggesting a positive thermal gradient with depth. The substantial degree of crystallisation estimated by trace element concentrations contrasts with the homogeneity of major element concentrations in MIs, which yield compositions closer to those of pumice whole rocks of the most evolved horizon, KF176_C (**Fig. 7**). This suggests that haüyne started crystallising quite lately and mostly entrapped a residual melt at late stages of chemical evolution. Sealed melt inclusions in haüyne crystals sampled in the deepest portions of the magmatic reservoir are on average slightly richer in K_2O and poorer in Na_2O compared to the topmost reservoir zones and open embayments (**Fig. 8c**). A preferential uptake of sodium relative to potassium indicates a less advanced stage of feldspar evolution at depth in the magmatic reservoir, which is then progressively balanced in open embayments with the progressive maturation of magma chemistry.

5.1.3 Water content

Water content in RP's melt inclusions is relatively lower than the estimated volatile content at saturation for phonolitic magmas at crustal levels (e.g., ~8 wt.% at 200 MPa; Carroll and Blank, 1997; Berndt et al., 2001) or values previously recorded in EAR peralkaline magmas (e.g., Wilding et al., 1993; Iddon and Edmonds, 2020), but is in agreement with undersaturated values of other phonolitic magmas hosting modal haüyne (e.g., El Abrigo ignimbrite at Tenerife, Spain; Andújar et al., 2008). The water concentrations are consistent in MIs and do not shift much from the average of 2.85 wt.%. A strong coherence is shown between MIs entrapped in a more external or internal portion of the same crystal (i.e., relative standard deviation ~6%), meaning

867 that even if MIs sampled different portions of the reservoir during the crystal migration, the
868 magma was homogeneous in its water content (Peppard et al., 2001). However, some outliers
869 above the first upper standard deviation (~3.7 wt.%) are found, mostly in horizons G and O.
870 We can therefore infer that water concentrations in the magma were homogeneously below
871 saturation at given pressure and temperature conditions, however, some localised portions of
872 the reservoir were more hydrated up to saturation as suggested by the presence of a pre-
873 entrapment fluid phase in some MIs (e.g., Dunbar and Hervig, 1992). Embayments yield on
874 average less water than sealed inclusions because melt in open embayments progressively
875 equilibrates with the surrounding melt during ascent and is more likely to experience a
876 diffusion-controlled re-equilibration during syn-eruptive degassing (Liu et al., 2007). We are
877 aware that diffusive loss of hydrogen through the crystal at magmatic temperatures might also
878 promote an equilibration of OH^- content in MIs with the external melt during magmatic
879 evolution (Esposito et al., 2014; Cannatelli et al., 2016 and reference therein). However, we
880 infer that melt was trapped in haüyne shortly before the eruption, in a steady shallow magmatic
881 reservoir and most likely a substantial degassing occurred during the eventual eruption, too fast
882 for the water content to be fully equilibrated. Additionally, no correlation exists between
883 location within the crystal, MI size and water content, making us confident that the latter was
884 not modified after trapping (Esposito et al., 2014).

885 Modelling of shrinking bubble formation during post-entrapment crystallisation suggests that a
886 considerable amount of water can be taken up in the bubble if no separated vapour phase is
887 present at the moment of entrapment, meaning that MIs are not always representative of water
888 content in the parental magma (Steele-MacInnis et al., 2017). Even though we expect no pre-
889 existing vapour entrapped in single-bubble MIs from our dataset, as argued above, we exclude
890 that post-entrapment crystallisation occurred. Additionally, we observe that water content
891 within bubble-free MIs is statistically equivalent to water content within MIs hosting a single

bubble (on average 2.89 ± 0.97 wt.% and 2.81 ± 0.55 wt.% respectively) whereas a larger variability (i.e., first standard deviation) is shown by bubble-free MIs because of a few outliers. Therefore, we are confident that the shrinkage bubble, when formed, mostly captured insoluble CO_2 from the melt. Previous studies of shrinkage bubbles revealed that these can yield between 30% and 90% of the originally total dissolved CO_2 (Esposito et al., 2011; Moore et al., 2015; Rose-Koga et al., 2021 and references therein; Feignon et al., 2022) marking their importance when assessing total CO_2 concentrations in MIs. No absorbance peak for the molecular CO_2 overtone at 2351 cm^{-1} (Brooker et al., 1999) was shown in the FTIR spectra collected, even for the thickest MIs, implying that CO_2^{mol} in the glass must be below the thickness-dependent detection limit of tens up to a hundred ppm (von Aulock et al., 2014; Rose-Koga et al., 2021). For lower silica and depolymerised melts, dissolved carbonate species (CO_3^{2-}) prevail over CO_2^{mol} in C-O species speciation (Brooker et al., 1999; Morizet et al., 2013) and produce an absorption doublet between 1670 and 1375 cm^{-1} (Brooker et al., 1999). Most of our IR spectra are particularly noisy below 1600-1550 cm^{-1}, and those spectra having a good signal-to-noise do not show any evident doublet, which can also be masked by the H_2O_{mol} peak at 1650 cm^{-1}. Dissolved CO_2 concentrations cannot be estimated for bubble-free MIs as well, suggesting that the amount of CO_2 uptake in shrinkage bubbles is overall limited. However, we claim that enough CO_2 was dissolved in the parental melt to allow the crystallisation of CO_2-rich haüyne and that possibly the current method was not capable of detecting it. Potentially, CO_2 loss might have occurred through diffusion within the host crystal, however, we do not have enough constraints about such a process and further investigations such as mapping of CO_2 concentrations in the host around the MIs or investigation of MIs hosted in CO_2-free crystalline phases would be required.

5.2 Thermobarometry

916 Entrapment temperatures estimated with the K-feldspar hygrometer (Mollo et al., 2015) are
917 substantially higher (i.e., percentage difference 13 ± 6% on average for MIs) and more dispersed
918 than those given by the alkali feldspar geothermometer (Putirka, 2008). The K-feldspar
919 hygrometer is strongly dependent on glass water estimations, and considering the related
920 estimated error, we prefer to rely on the glass chemistry-dependent alkali feldspar
921 geothermometer for further discussions. However, the equilibrium constant provided by Mollo
922 et al. (2015) was adopted as a further constraint to evaluate equilibrium between feldspars and
923 MI melts because the albite-anorthite test for equilibrium provided in Putirka (2008) is mostly
924 tested for plagioclase and has been only tested for alkali feldspar with 60 samples, resulting in
925 large standard deviations (Putirka, 2008).

926 Temperature estimations from MIs match the liquidus temperature estimated with rhyolite-
927 MELTS (Gualda et al., 2012a; Ghiorso and Gualda, 2015) at a given chemical composition and
928 lithostatic pressure. The progressive increase toward the bottom of the reservoir (**Fig. 6a**),
929 especially for the more dispersed distribution of MIs collected from horizon O, is interpreted to
930 be caused by the occurrence of both MIs entrapped at deeper portions of the reservoir and
931 shallower MIs entrapped in crystals that subsequently sunk in the reservoir because of density
932 gradients and convective motions.

933 A wide range of pressures can be recorded by MIs entrapped in crystals at different depths or
934 by MIs (or MIAs) entrapped in the same crystal at different times during their ascent or sinking
935 in the reservoir (Anderson et al., 2000; Peppard et al., 2001; Métrich and Wallace, 2008).
936 However, such constraints based on volatile variations in MIs must be interpreted carefully as
937 pressure estimations from solubility models can delineate a degassing path only in the case of
938 saturation. Furthermore, caution is required when interpreting depressurisation trends from
939 water estimates as artefacts can be introduced by the significant error in water determination
940 (Esposito et al., 2014). As we do not have any strong evidence for the saturation conditions

941 during the entrapment of bubble-free and single-bubble MIs, the pressures we estimated with
942 solubility models correspond to a minimum lithostatic pressure. This means that constraining a
943 degassing path is not possible. The pressures obtained from different deposit horizons are
944 similar, implying that even though these horizons might reflect different depths in the reservoir,
945 this information is not recorded in the estimated pressures because the water content is below
946 saturation. Similarly, MIs entrapped in the same crystals at different times and reservoir depths
947 did not preserve such information due to their homogeneity of water content below saturation.
948 Minimum lithostatic pressure skews around 55-65 MPa for all the solubility models considered,
949 implying a considerably shallow magmatic reservoir. Assuming an average continental crust
950 density of 2.7 $g \cdot cm^{-3}$, pressures from MIs can be converted to depths in the crust, which yield
951 an average depth of 2.47 ± 1.24 km and 2.35 ± 1.15 km for MooreWater and ShishkinaWater
952 models respectively. Even though the average depth given by the Iacono-MarzianoWater
953 solubility model gives a more realistic value (i.e., 6.95 ± 1.93 km depth), this model is mostly
954 calibrated for subalkaline and alkaline mafic magmatic compositions and therefore, might not
955 be appropriate for trachytic and phonolitic compositions. A calibration for broader compositions
956 is given for MagmaSat and MooreWater solubility models, whose results largely overlap.
957 Solubility experiments proved that such models might underestimate water solubility for
958 peralkaline trachytes and phonolites (Carroll and Blank, 1997; Di Matteo et al., 2004). This
959 effect is mainly attributed to the high concentration of alkaline elements, but it is observed only
960 at pressures higher than 50 MPa and considered significant over 200 MPa (Di Matteo et al.,
961 2004), meaning this underestimation might affect only to a minor extent our estimations.

962 Water contents in embayments are lower and so are the subordinate minimum pressure
963 estimations. The equilibration process of embayment melts with the external melt during syn-
964 eruptive degassing is correlated with element diffusivity and therefore, depending on ascent
965 rate, water content at different distances from the outlet within the embayment can record the

966 degassing path (Liu et al., 2007). We can assume that at least embayment portions at the outlet
967 were close to water saturation at the moment of quenching (deGraffenried and Shea, 2021;
968 Geshi et al., 2021), as also indicated by the formation of a large number of bubbles. This means
969 that lithostatic pressures estimated from embayments are closer to the true pressure values
970 which, however, correspond to the syn-eruptive water exsolution depth and not to the reservoir
971 storage depth. To avoid any border refraction, we collected FTIR spectra away from the outlet,
972 implying the possible overestimation of water saturation depths which are narrowly distributed
973 around 1.4 ± 0.4 km deep.

974 **5.3 Haüyne stability**

975 Despite haüyne crystals not showing any visible textural or chemical (in BSE imaging)
976 zonation, their chemistry across the stratigraphic section shows some progressive variation,
977 particularly for volatile species. The stability of haüyne in phonolitic melts from Laacher See
978 volcano (Germany) and Tenerife (Spain) has been experimentally constrained to oxidising
979 conditions (fO_2 > NNO buffer), pressures below 200-300 MPa, and temperatures between 750
980 and 900 °C (Berndt et al., 2001; Andújar et al., 2008; Baudouin and Parat, 2015). Haüyne
981 formed within the RP reservoir entrapped melt at shallower levels and slightly higher
982 temperatures. However, the sulphur content in RP magma is considerably higher than other
983 phonolitic systems in both haüyne (e.g., ~4 wt.% less in Laacher See phenocrysts; Berndt et al.,
984 2001) and melt (e.g., one order of magnitude lower in Laacher See MIs and matrix glasses;
985 Harms and Schmincke, 2000). This agrees with the experimental observation of Berndt et al.
986 (2001) that positively correlates the stability temperatures with sulphur availability and
987 oxidising conditions in the parental melt. The accessibility of sulphur thus likely plays an
988 important role in haüyne stability and growth rate (Harms and Schmincke, 2000; Berndt et al.,
989 2001; Cooper et al., 2015).

990 The ubiquitous occurrence of haüyne in the stratigraphic section from Laacher See, and the
991 composition of its MIs, let Berndt et al. (2001) imply a late differentiation of haüyne and
992 oxidising conditions likely shortly before the eruption due to the injection of a fresher and
993 oxidised magma. Sulphur sparging from depth is inferred to be one of the causes that promoted
994 the acceleration of haüyne growth in Tenerife (Spain) phonolites (Cooper et al., 2015). Sulphur
995 concentration in RP haüynes decreases ($\Delta_{SO3} \approx 2600$ ppm on average) toward the shallower
996 parts of the reservoir and is mirrored by a similar pattern in hosted MIs ($\Delta_{SO3} \approx 200$ ppm on
997 average) and tephra matrix ($\Delta_{SO3} \approx 400$ ppm). Among all the crystalline phases, the prolonged
998 uptake of sulphur in haüyne could potentially account for the depletion observed in the residual
999 melt at shallower depths (Harms and Schmincke, 2000). However, given the low modal
1000 proportions of crystallised haüyne (roughly estimated between 0.0 and 0.7 wt.%), it is unlikely
1001 that it alone was able to buffer sulphur content in the magma. Through a mass balance
1002 calculation, we estimated an extremely low (~38 ppm) sulphur uptake in haüyne in the topmost
1003 portions of the reservoir, while it is considerably more abundant in the deepest areas (600-800
1004 ppm) given the progressive increase of haüyne crystals there. Even though we inferred, to some
1005 extent, crystal migration within the reservoir, we would expect a higher sulphur content in
1006 haüyne formed in the reservoir cap, at least in the early-formed crystals. Sulphur loss might
1007 occur also due to exsolution in a fluid phase (Harms and Schmincke, 2000), but we do not have
1008 evidence for a separated fluid phase capping the reservoir, and on the contrary, MIs entrapped
1009 in the presence of a pre-entrapment fluid phase (i.e., microvesicular MIs) and MIs with
1010 anomalously higher water content, are more common at the reservoir bottom. All these
1011 instances indicate a higher haüyne stability in the deepest layer, which might be due to higher
1012 oxidised conditions and/or an input of sulphur from depth caused either by gas sparging (Cooper
1013 et al., 2015) or mixing/mingling with a more oxidised, sulphur-rich, magma (Harms and
1014 Schmincke, 2000; Berndt et al., 2001). These possible deep sources of volatiles were mostly

enriched in sulphur as other volatiles are constant (e.g., H_2O and CO_2) or show opposite trends (e.g., Cl^-) within haüyne and hosted MIs. Additionally, small grains of pyrrhotite were found included in alkali feldspar, biotite, and pyroxene (Fontijn et al., 2013), implying initial reducing conditions probably changed during haüyne crystallisation just prior to the eruption, similar to what observed at Laacher See phonolites (Berndt et al., 2001).

6 RESERVOIR CONCEPTUAL MODEL AND IMPLICATIONS

Pre-eruptive conditions for the Rungwe Pumice plumbing system obtained from geochemical data describe a relatively hot (~980 °C), phonolitic/peralkaline trachytic, magmatic reservoir ponded at shallow (≥ 2.2 km) depths below the surface. The pressures estimated with solubility models provide a minimum storage depth for an undersaturated melt, implying that magma could be stored at higher depths. However, we do not exclude that magma was indeed stored at shallow depths in the crust. Magma stored at such depths is considered unusual, however, petrological pieces of evidence, as well as factual observations (e.g., boreholes drilled in magma pockets at Krafla, Iceland, or Menengai, Kenya; Papale and Garg, 2022), showed that this might be more common than expected. Shallow depths are also inferred for other phonolitic systems in divergent, convergent or intraplate settings (e.g., Teide, Andújar et al., 2008; Andújar and Scaillet, 2012b; Vesuvius, Italy, Scaillet et al., 2008). Additionally, the CO_2 concentrations below FTIR detection limits in MIs suggested a prolonged magmatic degassing at crustal depth. Exsolved CO_2 may successfully escape the system and migrate upward and be emitted diffusively or in concentrated zones at the volcano's surface and surrounding areas. Differently from other volcanic systems along the rift hosting widespread hydrothermal systems (e.g., Hunt et al., 2017; Cappelli et al., 2023), gaseous emissions from present-day RVP are cold and enriched in CO_2 (Barry et al., 2013),

1038 The RP reservoir might have been separated and differentiated from a deeper basaltic parental
1039 magma (Furman, 1995) through fractional crystallisation (**Fig. 13a**). However, like at other
1040 peralkaline systems across the EAR where intermediate products are missing (e.g., Macdonald,
1041 1987; Tadesse et al., 2019 and references therein), we do not exclude that crustal assimilation
1042 processes contributed to some extent to magmatic differentiation, as also inferred by La/Nb
1043 values always above 1 (Plank, 2005). Once stored in the upper crust, a temperature gradient
1044 promoted crystal fractionation mostly at the shallower portions of the reservoir, crystallising
1045 mafic minerals (e.g., clinopyroxenes, biotite, and amphiboles in minor extent) and early alkali
1046 feldspars (**Fig. 13a**). Magmatic differentiation through fractional crystallisation proceeded
1047 consistently for quite some time, as implied by trace element patterns that suggest up to 50%
1048 fractional crystallisation and the size of some alkali feldspar crystals larger than 2 mm. Crystals
1049 formed at the topmost regions of the reservoir were most likely pushed toward reservoir walls
1050 and deeper regions, as inferred by the accumulation of alkali feldspars as free components at
1051 the highest horizons of the stratigraphic section and the corresponding enrichment in Ba (**Fig.**
1052 **13b**). However, as the crystal content in the ash components or within lapilli clasts is
1053 substantially low, and given the estimated degree of fractionation, it is plausible that only a
1054 small number of crystals formed this way were retained in the eruptible portion of the reservoir.
1055 Most crystals could have successfully segregated from the magma, as is modelled for crystal-
1056 poor rhyolitic magmas leaving behind batholitic crystalline mushes (Bachmann and Bergantz,
1057 2004) or inferred for other peralkaline systems within the EAR where mush segregation can be
1058 as fast as 10^{-1}-10^{-4} $km^3 \cdot yr^{-1}$ (Iddon et al., 2019).

1059 Convective motions might have partially homogenised the major element chemistry of the
1060 reservoir during haüyne crystallisation (**Fig. 13c**), which probably commenced at shallower
1061 crustal depths in comparison to mafic crystallisation as inferred by the different lithostatic
1062 pressures estimated in this study (i.e., 30-194 MPa) with those obtained from clinopyroxene-

liquid chemical stability (i.e., 70-350 MPa; Fontijn et al., 2013). Additionally, MIs hosted in biotite and clinopyroxenes yield more primitive compositions (Fontijn et al., 2013), suggesting a different time of entrapment. In any case, residence time at such shallower depths must have been relatively short, as indicated by the unfaceted shapes of MIs and the absence of breakdown or reaction rims around biotite crystals (Fontijn et al., 2013), unstable to depressurisation-induced water loss. However, given the original undersaturated conditions, an upward migration of RP's magmatic reservoir might have not directly caused water exsolution, preventing biotite breakdown (e.g., Fougnot et al., 1996).

Haüyne was probably stabilised in the deeper parts of the reservoir (horizon KF176_O) by more oxidising conditions. This could have been caused by either (1) the input of fresher, oxidised magma or (2) an SO_3-rich volatile phase sparging from depth, without a significant magma input. In case (1), the fresher magma must have yielded major element chemical concentrations close to the magma in the reservoir or have rested shorty in it (according to crystallisation kinetics), as no evident changes in alkali feldspars (or other phases) growth rims occur. Additionally, no strong compositional differences exist between tephra matrix glasses from different horizons and no evidence for magmatic mingling was found. The rare (<1% modal components) grey/banded pumice found in the lapilli grain size fraction (Fontijn et al., 2011) can be derived from local differences in crystallinity that were induced during magmatic ascent (Akin et al., 2024) since they do not have evident textural (vesicularity) or major oxide concentration differences (**Supplementary Table 3**). Evidence for (2), i.e. a volatile phase sparging from depth, comes from the preferential occurrence of microvesicular MIs within haüynes extracted from the bottom of the reservoir. The potential gaseous phases must have been rich in sulphur and depleted in other volatiles as the latter do not show any enrichment trends toward the reservoir bottom. Either a rapid accumulation of fresh magma or the input of external volatiles could potentially have a relevant role in destabilising the system and initiating

the unrest that culminated in an explosive eruption (**Fig. 13c,d**; e.g., Caricchi et al., 2018; Jorgenson et al., 2024).

By comparing parameters from several effusive and explosive eruptions from phonolitic-trachytic systems, Andújar and Scaillet (2012a) suggest that the relationship between water content and ponding depth significantly influences the eruptive behaviour of these magmas. While the proximity to water-saturation conditions is a relevant factor, water-saturation alone is not definitive in triggering explosive eruptions (Andújar and Scaillet, 2012a). In contrast, there does not appear to be a correlation between the rheological properties of these magmas and their eruptive dynamics. At a given temperature high-alkali silicic magmas yield viscosities more than one order of magnitude lower than their sub-alkaline counterparts (Di Genova et al., 2013). Low viscosities help decouple volatiles from magma and theoretically promote efficient outgassing and mildly explosive eruptions (Cassidy et al., 2018). However, at similar rheological conditions, peralkaline systems can experience either effusive or highly explosive eruptions (Andújar et al., 2008; Andújar and Scaillet, 2012a). For the RP magmas at storage conditions, we estimated an average viscosity of $10^{3.45 \pm 0.33}$ Pa·s (**Supplementary Table 2**) using the model of Giordano et al. (2008). At equivalent temperatures, such viscosity values are comparable to viscosities of phonolitic/trachytic melts from other explosive volcanic systems (Andújar and Scaillet, 2012a) but also to those of lathitic or shoshonitic magmas that produced strombolian or lava-fountaining activity (Di Genova et al., 2013). Volatile loss during magma ascent significantly impacts its viscosity. However, for RP magmas, the decrease in water content toward anhydrous conditions increases melt viscosity by a maximum of four orders of magnitude (up to 10^6 Pa·s). Despite this rise, viscosities remain below the threshold generally associated with brittle fragmentation (> 10^8 Pa·s; Papale, 1999). Additionally, the matrix glass of RP pumice clasts is aphyric and contains a limited amount of phenocrysts, indicating that crystallinity was most likely irrelevant to the magma's rheology (Dingwell et al., 1993). Water

content in the RP reservoir was low, likely below saturation, but considerably close to it. Additionally, the elevated bubble number density (Cappelli L, unpublished data) in pumice clasts suggests that rapid syn-eruptive bubble nucleation significantly influenced magma rheology. Consequently, conduit dynamics might have had a pivotal control in preventing outgassing and leading to brittle magma fragmentation, as suggested for other "low-viscosity" explosive eruptions (e.g., Houghton et al., 2004; Hughes et al., 2017).

We suggest that the RP magma was stored at sallow depths in conditions close to saturation. A gaseous phase sparging from deeper magmas entered the reservoir, induced haüyne crystallisation and likely destabilised the system. Shortly after, as inferred by unfaceted haüyne-hosted MIs, the eruption started. Once the eruption initiated, the magma rose rapidly and suddenly degassed producing the coeval homogeneous nucleation of a multitude of unconnected bubbles which hindered outgassing and promoted explosivity. Further investigations of conduit dynamics are required to unravel the degassing and fragmentation processes that ultimately determined the magma's behaviour, beyond the characteristics initially acquired at the reservoir level.

Across the East African Rift, several peralkaline silicic systems produced violent eruptions that sometimes culminated in caldera-forming events (e.g., Leat, 1984; Macdonald and Scaillet, 2006; White et al., 2012) but also showed less violent effusive activity associated with similar magmatic compositions. Although the eruptive volume of such explosive eruptions is generally modest (~1 km^3 DRE max) compared to arc magmatism, the transitional nature of these systems still poses a significant threat to such densely populated regions. Here, we state the importance of comprehensively describing the pre-eruptive conditions of such volcanic systems as single parameters such as water content or magma viscosity might be insufficient to predict the eruption style, and on the contrary, may lead to underestimating the explosive potentiality of the volcanic system.

DATA AVAILABILITY STATEMENT

The data underlying this article are available in the article and in its supplementary material.

FUNDING

This work was supported by an F.R.S.-FNRS Aspirant PhD studentship awarded to LC, and n F.R.S.-FNRS MIS [grant number F4515.20] awarded to KF. Samples were obtained during KF's doctoral thesis, funded by FWO Flanders. PW was founded by a F.R.S.-FNRS postdoctoral research fellowship. Isterre MicroAnalytical Plateforme (IMAP) in University Grenoble Alpes was funded by grants from: the European Research Council (ERC) under the European Union's Horizon H2020 research and innovation program (Synergy Grant MEET, grant agreement no.856555); Auvergne-Rhône-Alpes region (2020 AURA P3 - CPER 2015/2020).

ACKNOWLEDGEMENTS

The authors are grateful to Valentina Batanova and Valerie Magnin (IMAP laboratories, University Grenoble Alpes-Isterre; France) for technical support during EPMA data collection, Vinciane Debaille and Wendy Debouge (G-Time laboratory, Université Libre de Bruxelles; Belgium) for handling the mass spectrometry analyses and Aneta Slodczyk (CNRS-Orleans; France) for her assistance in FTIR analyses.

REFERENCES

Agrinier, P., Jendrzejewski, N., 2000. Overcoming problems of density and thickness measurements in FTIR volatile determinations: a spectroscopic approach. Contribution to Mineralogy and Petrology 139, 265–272.

1160 Akin, L., Aydar, E., Ceylan, A., 2024. A deep insight into a chemically homogeneous banded
1161 pumice sample: a role of crystal cargo immiscibility. Turkish Journal of Earth Sciences
1162 33, 341–361. https://doi.org/10.55730/1300-0985.1915

1163 Anderson, A.T., Davis, A.M., Lu, F., 2000. Evolution of Bishop Tuff Rhyolitic Magma Based
1164 on Melt and Magnetite Inclusions and Zoned Phenocrysts. Journal of Petrology 41, 449–
1165 473.

1166 Andújar, J., Costa, F., Martí, J., Wolff, J.A., Carroll, M.R., 2008. Experimental constraints on
1167 the pre-eruptive conditions of the phonolitic magma from the caldera-forming the Abrigo
1168 eruption, Tenerife (Canary Islands). Chemical Geology 257, 173–191.
1169 https://doi.org/10.1016/j.chemgeo.2008.08.012

1170 Andújar, J., Scaillet, B., 2012a. Relationships between pre-eruptive conditions and eruptive
1171 styles of phonolite-trachyte magmas. Lithos 152, 122–131.
1172 https://doi.org/10.1016/j.lithos.2012.05.009

1173 Andújar, J., Scaillet, B., 2012b. Experimental constraints on parameters controlling the
1174 difference in the eruptive dynamics of phonolitic magmas: The case of Tenerife (Canary
1175 Islands). Journal of Petrology 53, 1777–1806. https://doi.org/10.1093/petrology/egs033

1176 Bachmann, O., Bergantz, G.W., 2004. On the origin of crystal-poor rhyolites: Extracted from
1177 batholithic crystal mushes. Journal of Petrology 45, 1565–1582.
1178 https://doi.org/10.1093/petrology/egh019

1179 Barry, P.H., Hilton, D.R., Fischer, T.P., de Moor, J.M., Mangasini, F., Ramirez, C., 2013. Helium
1180 and carbon isotope systematics of cold “mazuku” CO2 vents and hydrothermal gases and
1181 fluids from Rungwe Volcanic Province, southern Tanzania. Chemical Geology 339, 141–
1182 156. https://doi.org/10.1016/j.chemgeo.2012.07.003

1183 Baudouin, C., Parat, F., 2015. Role of volatiles (S, Cl, H2O) and silica activity on the
1184 crystallization of haüyne and nosean in phonolitic magmas (Eifel, Germany and Saghro,
1185 Morocco). American Mineralogist 100, 2308–2322. https://doi.org/10.2138/am-2015-
1186 5318

1187 Behrens, H., Hahn, M., 2009. Trace element diffusion and viscous flow in potassium-rich
1188 trachytic and phonolitic melts. Chemical Geology 259, 63–77.
1189 https://doi.org/10.1016/j.chemgeo.2008.10.014

1190 Bellatreccia, F., Della Ventura, G., Piccinini, M., Cavallo, A., Brilli, M., 2009. H 2 O and CO 2
1191 in minerals of the haüyne-sodalite group: an FTIR spectroscopy study. Mineralogical
1192 Magazine 73, 399–413. https://doi.org/10.1180/minmag.2009.073.3.399

1193 Berndt, J., Holtz, F., Koepke, J., 2001. Experimental constraints on storage conditions in the
1194 chemically zoned phonolitic magma chamber of the Laacher See volcano. Contributions
1195 to Mineralogy and Petrology 140, 469–486.

1196 Biggs, J., Ayele, A., Fischer, T.P., Fontijn, K., Hutchison, W., Kazimoto, E., Whaler, K., Wright,
1197 T.J., 2021. Volcanic activity and hazard in the East African Rift Zone. Nature
1198 Communications. https://doi.org/10.1038/s41467-021-27166-y

1199 Bodnar, J.R., Student, J.J., 2006. Melt inclusions in plutonic rocks: Petrography and
1200 microthermometry, in: James D. Webster (Ed.), Melt Inclusions in Plutonic Rocks. Short
1201 course Vol.36, Mineralogical Association of Canada, Montreal, Quebec, pp. 1–25.

1202 Brooker, R.A., Kohn, S.C., Holloway, J.R., Mcmillan, P.F., Carroll, M.R., 1999. Solubility,
1203 speciation and dissolution mechanisms for CO_2 in melts on the $NaAlO_2$-SiO_2 join.
1204 Geochimica and Cosmochimica Acta 63, 3549–3565.

Cannatelli, C., Doherty, A.L., Esposito, R., Lima, A., De Vivo, B., 2016. Understanding a volcano through a droplet: A melt inclusion approach. Journal of Geochemical Exploration 171, 4–19. https://doi.org/10.1016/j.gexplo.2015.10.003

Cappelli, L., Wallace, P.A., Randazzo, A., Kamau, P.M., Njoroge, R.W., Otieno, V., Tubula, M.S., Mariita, N.O., Mangi, P., Fontijn, K., 2023. Diffuse soil CO2 emissions at rift volcanoes: Structural controls and total budget of the Olkaria Volcanic Complex (Kenya) case study. Journal of Volcanology and Geothermal Research 443. https://doi.org/10.1016/j.jvolgeores.2023.107929.

Carey, S., Sparks, R.S.J., 1986. Quantitative models of the fallout and dispersal of tephra from volcanic eruption columns. Bulletin of Volcanology 48, 109–125. https://doi.org/10.1007/BF01046546

Caricchi, L., Sheldrake, T.E., Blundy, J., 2018. Modulation of magmatic processes by CO2 flushing. Earth and Planetary Science Letters 491, 160–171. https://doi.org/10.1016/j.epsl.2018.03.042

Carroll, M.R., Blank, J.G., 1997. The solubility of H_2O in phonolitic melts, American Mineralogist.

Cassidy, M., Manga, M., Cashman, K., Bachmann, O., 2018. Controls on explosive-effusive volcanic eruption styles. Nature Communications 9. https://doi.org/10.1038/s41467-018-05293-3

Castillo, P.R., Hilton, D.R., Halldórsson, S.A., 2014. Trace element and Sr-Nd-Pb isotope geochemistry of Rungwe Volcanic Province, Tanzania: Implications for a superplume source for East Africa Rift magmatism. Frontiers in Earth Sciences 2. https://doi.org/10.3389/feart.2014.00021

1228 Cioni, R., 2000. Volatile content and degassing processes in the AD 79 magma chamber at
1229 Vesuvius (Italy). Contributions to Mineralogy and Petrology 140, 40–54.
1230 https://doi.org/10.1007/s004100000167

1231 Cioni, R., Santacroce, R., Sbrana, A., 1999. Pyroclastic deposits as a guide for reconstructing
1232 the multi-stage evolution of the Somma-Vesuvius Caldera. Springer-Verlag.

1233 Cooper, L.B., Bachmann, O., Huber, C., 2015. Volatile budget of Tenerife phonolites inferred
1234 from textural zonation of S-rich haüyne. Geology 43, 423–426.
1235 https://doi.org/10.1130/G36505.1

1236 Danyushevsky, L. V., McNeill, A.W., Sobolev, A. V., 2002. Experimental and petrological
1237 studies of melt inclusions in phenocrysts from mantle-derived magmas: An overview of
1238 techniques, advantages and complications. Chemical Geology 183, 5–24.
1239 https://doi.org/10.1016/S0009-2541(01)00369-2

1240 Davidson, P., Kamenetsky, V.S., 2007. Primary aqueous fluids in rhyolitic magmas: Melt
1241 inclusion evidence for pre- and post-trapping exsolution. Chemical Geology 237, 372–
1242 383. https://doi.org/10.1016/j.chemgeo.2006.07.009

1243 deGraffenried, R.L., Shea, T., 2021. Using Volatile Element Concentration Profiles in Crystal-
1244 Hosted Melt Embayments to Estimate Magma Decompression Rate: Assumptions and
1245 Inherited Errors. Geochemistry, Geophysics, Geosystems 22.
1246 https://doi.org/10.1029/2021GC009672.

1247 Degruyter, W., Bachmann, O., Burgisser, A., Manga, M., 2012. The effects of outgassing on the
1248 transition between effusive and explosive silicic eruptions. Earth and Planetary Science
1249 Letters 349–350, 161–170. https://doi.org/10.1016/j.epsl.2012.06.056

1250 Devine, J.D., Gardner, J.E., Brack, H.P., Layne, G.D., Rutherford, M.J., 1995. Comparison of
1251 microanalytical methods for estimating H2O contents of silicic volcanic glasses.
1252 American Mineralogist 80, 319–328. https://doi.org/10.2138/am-1995-3-413

1253 Di Genova, D., Romano, C., Hess, K.U., Vona, A., Poe, B.T., Giordano, D., Dingwell, D.B.,
1254 Behrens, H., 2013. The rheology of peralkaline rhyolites from Pantelleria Island. Journal
1255 of Volcanology and Geothermal Research 249, 201–216.
1256 https://doi.org/10.1016/j.jvolgeores.2012.10.017

1257 Di Matteo, V., Carroll, M.R., Behrens, H., Vetere, F., Brooker, R.A., 2004. Water solubility in
1258 trachytic melts. Chemical Geology 213, 187–196.
1259 https://doi.org/10.1016/j.chemgeo.2004.08.042

1260 Dingwell, D.B., 1996. Volcanic Dilemma: Flow or Blow? Science (1979) 273, 1054–1055.

1261 Dingwell, D.B., Bagdassarov, N.S., Bussod, G.Y., Webb, S.L., 1993. Magma Rheology, in:
1262 Luth, R.W. (Ed.), Experiments at High Pressures and Applications to the Earth's Mantle,
1263 Short Course Handbook. Mineralogical Association of Canada, Edmonton, Alberta, pp.
1264 131–196.

1265 Dingwell, D.B., Webb, S.L., 1989. Structural Relaxation in Silicate Melts and Non-Newtonian
1266 Melt Rheology in Geologic Processes. Physics and Chemistry of Minerals 16, 508–516.

1267 Dunbar, N.W., Hervig, R.L., 1992. Volatile and trace element composition of melt inclusions
1268 from the Lower Bandelier Tuff: implications for magma chamber processes and eruptive
1269 style. Journal of Geophysical Research 97, 15151-15170.
1270 https://doi.org/10.1029/92jb01340

1271 Ebinger, C., 2005. Continental break-up: The East African perspective. Astronomy and
1272 Geophysics 46, 2.16-2.21. https://doi.org/10.1111/j.1468-4004.2005.46216.x

1273 Ebinger, C.J., Deino, A.L., Drake, E., Tesha, A.L., 1989. Chronology of volcanism and rift basin
1274 propagation: Rungwe Volcanic Province, East Africa. Journal of Geophysical Research
1275 94, 15785–15803.

1276 Ebinger, C.J., Deino, A.L., Tesha, A.L., Becker, T., Ring, U., 1993. Tectonic controls on rift
1277 basin morphology: evolution of the northern Malawi (Nyasa) Journal of Geophysical
1278 Research 98, 17821-17836. https://doi.org/10.1029/93jb01392

1279 Ebinger, C.J., Keir, D., Bastow, I.D., Whaler, K., Hammond, J.O.S., Ayele, A., Miller, M.S.,
1280 Tiberi, C., Hautot, S., 2017. Crustal Structure of Active Deformation Zones in Africa:
1281 Implications for Global Crustal Processes. Tectonics 36, 3298-3332.
1282 https://doi.org/10.1002/2017TC004526

1283 Esposito, R., Bodnar, R.J., Danyushevsky, L. V., De vivo, B., Fedele, L., Hunter, J., Lima, A.,
1284 Shimizu, N., 2011. Volatile evolution of magma associated with the Solchiaro eruption in
1285 the Phlegrean Volcanic District (Italy). Journal of Petrology 52, 2431–2460.
1286 https://doi.org/10.1093/petrology/egr051

1287 Esposito, R., Hunter, J., Schiffbauer, J.D., Shimizu, N., Bodnar, R.J., 2014. An assessment of
1288 the reliability of melt inclusions as recorders of the pre-eruptive volatile content of
1289 magmas. American Mineralogist 99, 976–998. https://doi.org/10.2138/am.2014.4574

1290 Esposito, R., Klebesz, R., Bartoli, O., Klyukin, Y.I., Moncada, D., Doherty, A.L., Bodnar, R.J.,
1291 2012. Application of the linkam TS1400XY heating stage to melt inclusion studies.
1292 Central European Journal of Geosciences 4(2), 208–218. https://doi.org/10.2478/s13533-
1293 011-0054-y

1294 Faure, F., Schiano, P., 2005. Experimental investigation of equilibration conditions during
1295 forsterite growth and melt inclusion formation. Earth and Planetary Science Letters 236,
1296 882–898. https://doi.org/10.1016/j.epsl.2005.04.050

1297 Feignon, J.G., Cluzel, N., Schiavi, F., Moune, S., Roche, O., Clavero, J., Schiano, P., Auxerre,
1298 M., 2022. High CO2 content in magmas of the explosive andesitic Enco eruption of
1299 Mocho-Choshuenco volcano (Chile). Bulletin of Volcanology 84.
1300 https://doi.org/10.1007/s00445-022-01550-y

1301 Fontijn, K., Delvaux, D., Ernst, G.G.J., Kervyn, M., Mbede, E., Jacobs, P., 2010a. Tectonic
1302 control over active volcanism at a range of scales: Case of the Rungwe Volcanic Province,
1303 SW Tanzania; and hazard implications. Journal of African Earth Sciences 58, 764–777.
1304 https://doi.org/10.1016/j.jafrearsci.2009.11.011

1305 Fontijn, K., Elburg, M.A., Nikogosian, I.K., van Bergen, M.J., Ernst, G.G.J., 2013. Petrology
1306 and geochemistry of Late Holocene felsic magmas from Rungwe volcano (Tanzania),
1307 with implications for trachytic Rungwe Pumice eruption dynamics. Lithos 177, 34–53.
1308 https://doi.org/10.1016/j.lithos.2013.05.012

1309 Fontijn, K., Ernst, G.G.J., Bonadonna, C., Elburg, M.A., Mbede, E., Jacobs, P., 2011. The ~4-
1310 ka Rungwe Pumice (South-Western Tanzania): A wind-still Plinian eruption. Bulletin of
1311 Volcanology 73, 1353–1368. https://doi.org/10.1007/s00445-011-0486-8

1312 Fontijn, K., Ernst, G.G.J., Elburg, M.A., Williamson, D., Abdallah, E., Kwelwa, S., Mbede, E.,
1313 Jacobs, P., 2010b. Holocene explosive eruptions in the Rungwe Volcanic Province,
1314 Tanzania. Journal of Volcanology and Geothermal Research 196, 91–110.
1315 https://doi.org/10.1016/j.jvolgeores.2010.07.021

1316 Fontijn, K., McNamara, K., Zafu Tadesse, A., Pyle, D.M., Dessalegn, F., Hutchison, W., Mather,
1317 T.A., Yirgu, G., 2018. Contrasting styles of post-caldera volcanism along the Main
1318 Ethiopian Rift: Implications for contemporary volcanic hazards. Journal of Volcanology
1319 and Geothermal Research 356, 90–113. https://doi.org/10.1016/j.jvolgeores.2018.02.001

1320 Fontijn, K., Williamson, D., Mbede, E., Ernst, G.G.J., 2012. The Rungwe Volcanic Province,
1321 Tanzania - A volcanological review. Journal of African Earth Sciences 63, 12–31.
1322 https://doi.org/10.1016/j.jafrearsci.2011.11.005

1323 Fougnot, J., Pichavant, M., Barbey, P., 1996. Biotite resorption in dacite lavas from northeastern
1324 Algeria. European Journal of Mineralogy 8, 625–638.

1325 Furman, T., 1995. Melting of metasomatized subcontinental lithosphere: undersaturated mafic
1326 lavas from Rungwe, Tanzania, Contrib Mineral Petrol. Springer-Verlag.

1327 Garcin, Y., Williamson, D., Taieb, M., Vincens, A., Mathé, P.E., Majule, A., 2006. Centennial
1328 to millennial changes in maar-lake deposition during the last 45,000 years in tropical
1329 Southern Africa (Lake Masoko, Tanzania). Palaeogeography, Palaeoclimatology,
1330 Palaeoecology 239, 334–354. https://doi.org/10.1016/j.palaeo.2006.02.002

1331 Geshi, N., Yamasaki, T., Miyagi, I., Conway, C.E., 2021. Magma chamber decompression
1332 during explosive caldera-forming eruption of Aira caldera. Communications Earth &
1333 Environment 2. https://doi.org/10.1038/s43247-021-00272-x

1334 Ghiorso, M.S., Evans, B.W., 2008. Thermodynamics of rhombohedral oxide solid solutions and
1335 a revision of the Fe-Ti two-oxide geothermometer and oxygen-barometer. American
1336 Journal of Science 308, 957–1039. https://doi.org/10.2475/09.2008.01

1337 Ghiorso, M.S., Gualda, G.A.R., 2015. An H2O–CO2 mixed fluid saturation model compatible
1338 with rhyolite-MELTS. Contributions to Mineralogy and Petrology 169.
1339 https://doi.org/10.1007/s00410-015-1141-8

1340 Giordano, D., Russell, J.K., Dingwell, D.B., 2008. Viscosity of magmatic liquids: A model.
1341 Earth and Planetary Science Letters 271, 123–134.
1342 https://doi.org/10.1016/j.epsl.2008.03.038

1343 Gualda, G.A.R., Ghiorso, M.S., Lemons, R. V., Carley, T.L., 2012a. Rhyolite-MELTS: A
1344 modified calibration of MELTS optimized for silica-rich, fluid-bearing magmatic
1345 systems. Journal of Petrology 53, 875–890. https://doi.org/10.1093/petrology/egr080

1346 Gualda, G.A.R., Pamukcu, A.S., Ghiorso, M.S., Anderson, A.T., Sutton, S.R., Rivers, M.L.,
1347 2012b. Timescales of Quartz crystallization and the longevity of the Bishop Giant Magma
1348 body. PLOS One 7. https://doi.org/10.1371/journal.pone.0037492

1349 Harkin, D.A., 1960. The Rungwe Volcanics at the Northern End of Lake Nyasa, 1st ed.
1350 Government Printer.

1351 Harms, E., Schmincke, H.-U., 2000. Volatile composition of the phonolitic Laacher See magma
1352 (12,900 yr BP): implications for syn-eruptive degassing of S, F, Cl and H 2 O.
1353 Contributions to Mineralogy and Petrology 138, 84–98.

1354 Hosseini, B., Myers, M.L., Watkins, J.M., Harris, M.A., 2023. Are We Recording? Putting
1355 Embayment Speedometry to the Test Using High Pressure-Temperature Decompression
1356 Experiments. Geochemistry, Geophysics, Geosystems 24.
1357 https://doi.org/10.1029/2022gc010770

1358 Houghton, B.F., Wilson, C.J.N., Del Carlo, P., Coltelli, M., Sable, J.E., Carey, R., 2004. The
1359 influence of conduit processes on changes in style of basaltic Plinian eruptions: Tarawera
1360 1886 and Etna 122 BC. Journal of Volcanology and Geothermal Research 137, 1–14.
1361 https://doi.org/10.1016/j.jvolgeores.2004.05.009

1362 Huber, C., Townsend, M., Degruyter, W., Bachmann, O., 2019. Optimal depth of subvolcanic
1363 magma chamber growth controlled by volatiles and crust rheology. Nature Geosciences
1364 12, 762–768. https://doi.org/10.1038/s41561-019-0415-6

1365 Hughes, E.C., Neave, D.A., Dobson, K.J., Withers, P.J., Edmonds, M., 2017. How to fragment
1366 peralkaline rhyolites: Observations on pumice using combined multi-scale 2D and 3D
1367 imaging. Journal of Volcanology and Geothermal Research 336, 179–191.
1368 https://doi.org/10.1016/j.jvolgeores.2017.02.020

1369 Hunt, J.A., Zafu, A., Mather, T.A., Pyle, D.M., Barry, P.H., 2017. Spatially Variable CO2
1370 Degassing in the Main Ethiopian Rift: Implications for Magma Storage, Volatile
1371 Transport, and Rift-Related Emissions. Geochemistry, Geophysics, Geosystems 18,
1372 3714–3737. https://doi.org/10.1002/2017GC006975

1373 Hutchison, W., Mather, T.A., Pyle, D.M., Boyce, A.J., Gleeson, M.L.M., Yirgu, G., Blundy,
1374 J.D., Ferguson, D.J., Vye-Brown, C., Millar, I.L., Sims, K.W.W., Finch, A.A., 2018. The
1375 evolution of magma during continental rifting: New constraints from the isotopic and
1376 trace element signatures of silicic magmas from Ethiopian volcanoes. Earth and Planetary
1377 Science Letters 489, 203–218. https://doi.org/10.1016/j.epsl.2018.02.027

1378 Hutchison, W., Pyle, D.M., Mather, T.A., Yirgu, G., Biggs, J., Cohen, B.E., Barfod, D.N., Lewi,
1379 E., 2016. The eruptive history and magmatic evolution of Aluto volcano: new insights
1380 into silicic peralkaline volcanism in the Ethiopian rift. Journal of Volcanology and
1381 Geothermal Research 328, 9–33. https://doi.org/10.1016/j.jvolgeores.2016.09.010

1382 Iacono-Marziano, G., Morizet, Y., Le Trong, E., Gaillard, F., 2012. New experimental data and
1383 semi-empirical parameterization of H_2O-CO_2 solubility in mafic melts. Geochimica et
1384 Cosmochimica Acta 97, 1–23. https://doi.org/10.1016/j.gca.2012.08.035

1385 Iacovino, K., Matthews, S., Wieser, P.E., Moore, G.M., Bégué, F., 2021. VESIcal Part I: An
1386 Open-Source Thermodynamic Model Engine for Mixed Volatile (H2O-CO2) Solubility
1387 in Silicate Melts. Earth and Space Science 8. https://doi.org/10.1029/2020EA001584

1388 Iddon, F., Edmonds, M., 2020. Volatile-Rich Magmas Distributed Through the Upper Crust in
1389 the Main Ethiopian Rift. Geochemistry, Geophysics, Geosystems 21.
1390 https://doi.org/10.1029/2019GC008904

1391 Iddon, F., Jackson, C., Hutchison, W., Fontijn, K., Pyle, D.M., Mather, T.A., Yirgu, G.,
1392 Edmonds, M., 2019. Mixing and Crystal Scavenging in the Main Ethiopian Rift Revealed
1393 by Trace Element Systematics in Feldspars and Glasses. Geochemistry, Geophysics,
1394 Geosystems 20, 230–259. https://doi.org/10.1029/2018GC007836

1395 Jochum, K.P., Stoll, B., Herwig, K., Willbold, M., Hofmiann, A.W., Amini, M., Aarburg, S.,
1396 Abouchami, W., Hellebrand, E., Mocek, B., Raczek, I., Stracke, A., Alard, O., Bouman,
1397 C., Becker, S., Dücking, M., Brätz, H., Klemd, R., De Bruin, D., Canil, D., Cornell, D.,
1398 De Hoog, C.J., Dalpé, C., Danyushevshy, L., Eisenhauer, A., Gao, Y., Snow, J.E.,
1399 Groschopf, N., Günther, D., Latkoczy, C., Guillong, M., Hauri, E.H., Höfer, H.E., Lahaye,
1400 Y., Horz, K., Jacob, D.E., Kasemann, S.A., Kent, A.J.R., Ludwig, T., Zack, T., Mason,
1401 P.R.D., Meixner, A., Rosner, M., Misawa, K., Nash, B.P., Pfänder, J., Premo, W.R., Sun,
1402 W.D., Tiepolo, M., Vannucci, R., Vennemann, T., Wayne, D., Woodhead, J.D., 2006. MPI-
1403 DING reference glasses for in situ microanalysis: New reference values for element
1404 concentrations and isotope ratios. Geochemistry, Geophysics, Geosystems 7.
1405 https://doi.org/10.1029/2005GC001060

1406 Jorgenson, C., Caricchi, L., Chiaradia, M., Ágreda-López, M., Giordano, G., 2024. Rapid
1407 accumulation and ascent precedes caldera forming eruption of low viscosity magma.
1408 Contributions to Mineralogy and Petrology 179. https://doi.org/10.1007/s00410-023-
1409 02091-z

1410 Keller, J., Ryan, W.B.F., Ninkovich, D., Altherr, R., 1978. Explosive volcanic activity in the
1411 Mediterranean over the past 200,000 yr as recorded in deep-sea sediments. Bulletin of the

Geological Society of America 89, 591–604. https://doi.org/10.1130/0016-7606(1978)89<591:EVAITM>2.0.CO;2

Kendall, J.M., Lithgow-Bertelloni, C., 2016. Why is Africa rifting?, in: Geological Society Special Publication. Geological Society of London, pp. 11–30. https://doi.org/10.1144/SP420.17

Keranen, K., Klemperer, S.L., Gloaguen, R., Asfaw, L., Ayele, A., Ebinger, C., Furman, T., Harder, S., Keler, G.R., Mackenzie, G.D., Maguire, P.K.H., Stuart, G.W., 2004. Three-dimensional seismic imaging of a protoridge axis in the Main Ethiopian rift. Geology 32, 949–952. https://doi.org/10.1130/G20737.1

Lange, R.A., 1997. A revised model for the density and thermal expansivity of K_2O-Na_2O-CaO-MgO-Al_2O_3-SiO_2 liquids from 700 to 1900 K: extension to crustal magmatic temperatures. Contributions to Mineralogy and Petrology 130, 1–11. https://doi.org/10.1007/s004100050345

Lange, R.A., Carmichael, I.S.E., 1987. Densities of Na_2O-K_2O-CaO-MgO-FeO-Fe_2O_3-Al_2O_3-TiO_2-SiO_2 liquids: New measurements and derivated partial molar properties. Geochimica et Cosmochimica Acta 51, 2931–2946.

Leat, P.T., 1984. Geological evolution of the trachytic caldera volcano Menengai, Kenya Rift Valley. Journal of the Geological Society of London 141, 1057–1069. https://doi.org/10.1144/gsjgs.141.6.1057

Liu, Y., Anderson, A.T., Wilson, C.J.N., 2007. Melt pockets in phenocrysts and decompression rates of silicic magmas before fragmentation. Journal of Geophysical Research: Solid Earth 112. https://doi.org/10.1029/2006JB004500

1434 Macdonald, R., 1987. Quaternary peralkaline silicic rocks and caldera volcanoes of Kenya.
1435 Geological Society Special Publication 30, 313–333.
1436 https://doi.org/10.1144/GSL.SP.1987.030.01.15

1437 Macdonald, R., Scaillet, B., 2006. The central Kenya peralkaline province: Insights into the
1438 evolution of peralkaline salic magmas. Lithos 91, 59–73.
1439 https://doi.org/10.1016/j.lithos.2006.03.009

1440 McDonough, W.F., Sun, S. -s., 1995. The Composition of Earth. Chemical Geology 120, 223–
1441 253.

1442 Métrich, N., Wallace, P.J., 2008. Volatile abundances in basaltic magmas and their degassing
1443 paths tracked by melt inclusions. Reviews in Mineralogy and Geochemistry 69, 363–402.
1444 https://doi.org/10.2138/rmg.2008.69.10

1445 Mollo, S., Masotta, M., Forni, F., Bachmann, O., De Astis, G., Moore, G., Scarlato, P., 2015. A
1446 K-feldspar-liquid hygrometer specific to alkaline differentiated magmas. Chemical
1447 Geology 392, 1–8. https://doi.org/10.1016/j.chemgeo.2014.11.010

1448 Moore, G., Vennemann, T., Carmichael, I.S.E., 1998. An empirical model for the solubility of
1449 H_2O in magmas to 3 kilobars, American Mineralogist 83, 1-2. https://doi.org/10.2138/am-
1450 1998-1-203

1451 Moore, L.R., Gazel, E., Tuohy, R., Lloyd, A.S., Esposito, R., Steele-MacInnis, M., Hauri, E.H.,
1452 Wallace, P.J., Plank, T., Bodnar, R.J., 2015. Bubbles matter: An assessment of the
1453 contribution of vapor bubbles to melt inclusion volatile budgets. American Mineralogist
1454 100, 806–823. https://doi.org/10.2138/am-2015-5036

1455 Morizet, Y., Brooker, R.A., Iacono-Marziano, G., Kjarsgaard, B.A., 2013. Quantification of
1456 dissolved CO_2 in silicate glasses using micro-Raman spectroscopy. American
1457 Mineralogist 98, 1788–1802. https://doi.org/10.2138/am.2013.4516

1458 Namur, O., Humphreys, M.C.S., 2018. Trace element constraints on the differentiation and
1459 crystal mush solidification in the Skaergaard intrusion, Greenland. Journal of Petrology
1460 59, 387–418. https://doi.org/10.1093/petrology/egy032

1461 Newhall, C.G., Self, S., 1982. The volcanic explosivity index (VEI): an estimate of the
1462 explosive magnitude for historical eruptions. Journal of Geophysical Research 87, 1231–
1463 1238.

1464 Nichols, A.R.L., Wysoczanski, R.J., 2007. Using micro-FTIR spectroscopy to measure volatile
1465 contents in small and unexposed inclusions hosted in olivine crystals. Chemical Geology
1466 242, 371–384. https://doi.org/10.1016/j.chemgeo.2007.04.007.

1467 Ochs III, F.A., Lange, R.A., 1999. The Density of Hydrous Magmatic Liquids. Science (1979)
1468 283, 1314–1317. https://doi.org/DOI: 10.1126/science.283.5406.1314.

1469 Pamukcu, A.S., Gualda, G.A.R., Bégué, F., Gravley, D.M., 2015. Melt inclusion shapes:
1470 Timekeepers of short-lived giant magma bodies. Geology 43, 947–950.
1471 https://doi.org/10.1130/G37021.1

1472 Papale, P., 1999. Strain-induced magma fragmentation in explosive eruptions. Nature 397, 425–
1473 428.

1474 Papale, P., Garg, D., 2022. Big volcano science: needs and perspectives. Bulletin of
1475 Volcanology 84. https://doi.org/10.1007/s00445-022-01524-0

1476 Peppard, B.T., Steele, I.M., Davis, A.M., Wallace, P.J., Anderson, A.T., 2001. Zoned quartz
1477 phenocrysts from the rhyolitic Bishop Tuff. American Mineralogist 86, 1034–1052.

1478 Plank, T., 2005. Constraints from Thorium/Lanthanum on sediment recycling at subduction
1479 zones and the evolution of the continents. Journal of Petrology 46, 921–944.
1480 https://doi.org/10.1093/petrology/egi005.

1481 Putirka, K.D., 2008. Thermometers and barometers for volcanic systems. Reviews in
1482 Mineralogy and Geochemistry 69, 61–120. https://doi.org/10.2138/rmg.2008.69.3.

1483 Richet, P., Whittington, A., Holtz, F., Behrens, H., Ohlhorst, S., Wilke, M., 2000. Water and the
1484 density of silicate glasses. Contributions to Mineralogy and Petrology 138, 337–347.
1485 https://doi.org/10.1007/s004100050567.

1486 Rose-Koga, E.F., Bouvier, A.S., Gaetani, G.A., Wallace, P.J., Allison, C.M., Andrys, J.A.,
1487 Angeles de la Torre, C.A., Barth, A., Bodnar, R.J., Bracco Gartner, A.J.J., Butters, D.,
1488 Castillejo, A., Chilson-Parks, B., Choudhary, B.R., Cluzel, N., Cole, M., Cottrell, E.,
1489 Daly, A., Danyushevsky, L. V., DeVitre, C.L., Drignon, M.J., France, L., Gaborieau, M.,
1490 Garcia, M.O., Gatti, E., Genske, F.S., Hartley, M.E., Hughes, E.C., Iveson, A.A., Johnson,
1491 E.R., Jones, M., Kagoshima, T., Katzir, Y., Kawaguchi, M., Kawamoto, T., Kelley, K.A.,
1492 Koornneef, J.M., Kurz, M.D., Laubier, M., Layne, G.D., Lerner, A., Lin, K.Y., Liu, P.P.,
1493 Lorenzo-Merino, A., Luciani, N., Magalhães, N., Marschall, H.R., Michael, P.J.,
1494 Monteleone, B.D., Moore, L.R., Moussallam, Y., Muth, M., Myers, M.L., Narváez, D.F.,
1495 Navon, O., Newcombe, M.E., Nichols, A.R.L., Nielsen, R.L., Pamukcu, A., Plank, T.,
1496 Rasmussen, D.J., Roberge, J., Schiavi, F., Schwartz, D., Shimizu, K., Shimizu, N.,
1497 Thomas, J.B., Thompson, G.T., Tucker, J.M., Ustunisik, G., Waelkens, C., Zhang, Y.,
1498 Zhou, T., 2021. Silicate melt inclusions in the new millennium: A review of recommended
1499 practices for preparation, analysis, and data presentation. Chemical Geology 570.
1500 https://doi.org/10.1016/j.chemgeo.2021.120145.

1501 Rowe, M.C., Lassiter, J.C., Goff, K., 2015. Basalt volatile fluctuations during continental
1502 rifting: An example from the Rio Grande Rift, USA. Geochemistry, Geophysics,
1503 Geosystems 16, 1254–1273. https://doi.org/10.1002/2014GC005649.

1504 Ruefer, A.C., Befus, K.S., Thompson, J.O., Andrews, B.J., 2021. Implications of Multiple
1505 Disequilibrium Textures in Quartz-Hosted Embayments. Frontiers in Earth Science 9.
1506 https://doi.org/10.3389/feart.2021.742895.

1507 Saria, E., Calais, E., Stamps, D.S., Delvaux, D., Hartnady, C.J.H., 2014. Present-day kinematics
1508 of the East African Rift. Journal of Geophysical Research: Solid Earth 119, 3584–3600.
1509 https://doi.org/10.1002/2013JB010901.

1510 Scaillet, B., MacDonald, R., 2001. Phase relations of peralkaline silicic magmas and
1511 petrogenetic implications. Journal of Petrology 42, 825–845.
1512 https://doi.org/10.1093/petrology/42.4.825.

1513 Scaillet, B., Pichavant, M., Cioni, R., 2008. Upward migration of Vesuvius magma chamber
1514 over the past 20,000 years. Nature 455, 216–219. https://doi.org/10.1038/nature07232

1515 Shishkina, T.A., Botcharnikov, R.E., Holtz, F., Almeev, R.R., Jazwa, A.M., Jakubiak, A.A.,
1516 2014. Compositional and pressure effects on the solubility of H_2O and CO_2 in mafic
1517 melts. Chemical Geology 388, 112–129. https://doi.org/10.1016/j.chemgeo.2014.09.001

1518 Sparks, R.S.J., 1978. The dynamics of bubble formation and growth in magmas: a review and
1519 analysis. Journal of Volcanology and Geothermal Research 3, 1–37.

1520 Steele-MacInnis, M., Esposito, R., Moore, L.R., Hartley, M.E., 2017. Heterogeneously
1521 entrapped, vapor-rich melt inclusions record pre-eruptive magmatic volatile contents.
1522 Contributions to Mineralogy and Petrology 172. https://doi.org/10.1007/s00410-017-
1523 1343-3

1524 Stolper, E., 1982. Water in silicate glasses: An infrared spectroscopic study. Contributions to
1525 Mineralogy and Petrology 81, 1–17. https://doi.org/10.1007/BF00371154.

1526 Tadesse, A.Z., Ayalew, D., Pik, R., Yirgu, G., Fontijn, K., 2019. Magmatic evolution of the
1527 Boku Volcanic Complex, Main Ethiopian Rift. Journal of African Earth Sciences 149,
1528 109–130. https://doi.org/10.1016/j.jafrearsci.2018.08.003.

1529 Taylor, D., 1967. The Sodalite Group of Minerals, Contributions to Mineralogy and Petrology
1530 16, 172-188.

1531 von Aulock, F.W., Kennedy, B.M., Schipper, C.I., Castro, J.M., E. Martin, D., Oze, C., Watkins,
1532 J.M., Wallace, P.J., Puskar, L., Bégué, F., Nichols, A.R.L., Tuffen, H., 2014. Advances in
1533 Fourier transform infrared spectroscopy of natural glasses: From sample preparation to
1534 data analysis. Lithos 206–207, 52–64. https://doi.org/10.1016/j.lithos.2014.07.017.

1535 Wadge, G., Biggs, J., Lloyd, R., Kendall, J.M., 2016. Historical volcanism and the state of stress
1536 in the East African Rift system. Frontiers in Earth Sciences 4.
1537 https://doi.org/10.3389/feart.2016.00086.

1538 White, J.C., Espejel-García, V. V., Anthony, E.Y., Omenda, P., 2012. Open System evolution of
1539 peralkaline trachyte and phonolite from the Suswa volcano, Kenya rift. Lithos 152, 84–
1540 104. https://doi.org/10.1016/j.lithos.2012.01.023.

1541 Wilding, M.C., Macdonald, R., Davies, J.E., Falliek, A.E., 1993. Volatile characteristics of
1542 peralkaline rhyolites from Kenya: an ion microprobe, infrared spectroscopic and
1543 hydrogen isotope study. Contributions to Mineralogy and Petrology 114, 26–275.

1544 Williams, L.A.J., Macdonald, R., Chapman, G.R., 1984. Late Quaternary caldera volcanoes of
1545 the Kenya Rift Valley. Journal of Geophysical Research 89, 8553–8570.
1546 https://doi.org/10.1029/JB089iB10p08553.

1547 Wysoczanski, R., Tani, K., 2006. Spectroscopic FTIR imaging of water species in silicic
1548 volcanic glasses and melt inclusions: An example from the Izu-Bonin arc. Journal of
1549 Volcanology and Geothermal Research 156, 302–314.
1550 https://doi.org/10.1016/j.jvolgeores.2006.03.024.

FIGURES

Fig. 1: **a)** Location of the Rungwe Volcanic Province (*yellow box*) at the junction between the Eastern and Western branches of the EAR. Major rift faults (*red lines*) and volcanoes (*grey triangles*) are indicated; **b)** shaded relief map of the RVP. The extension of the 25 cm isopach of the Rungwe Pumice fallout deposit is indicated by the red, dashed line (modified after Fontijn et al., 2011) while the location of the type section KF176 is indicated with the yellow symbol (12 m resolution DEM data: ASF DAAC, ALOS PALSAR_RTC_High res 2010; © JAXA/METI).

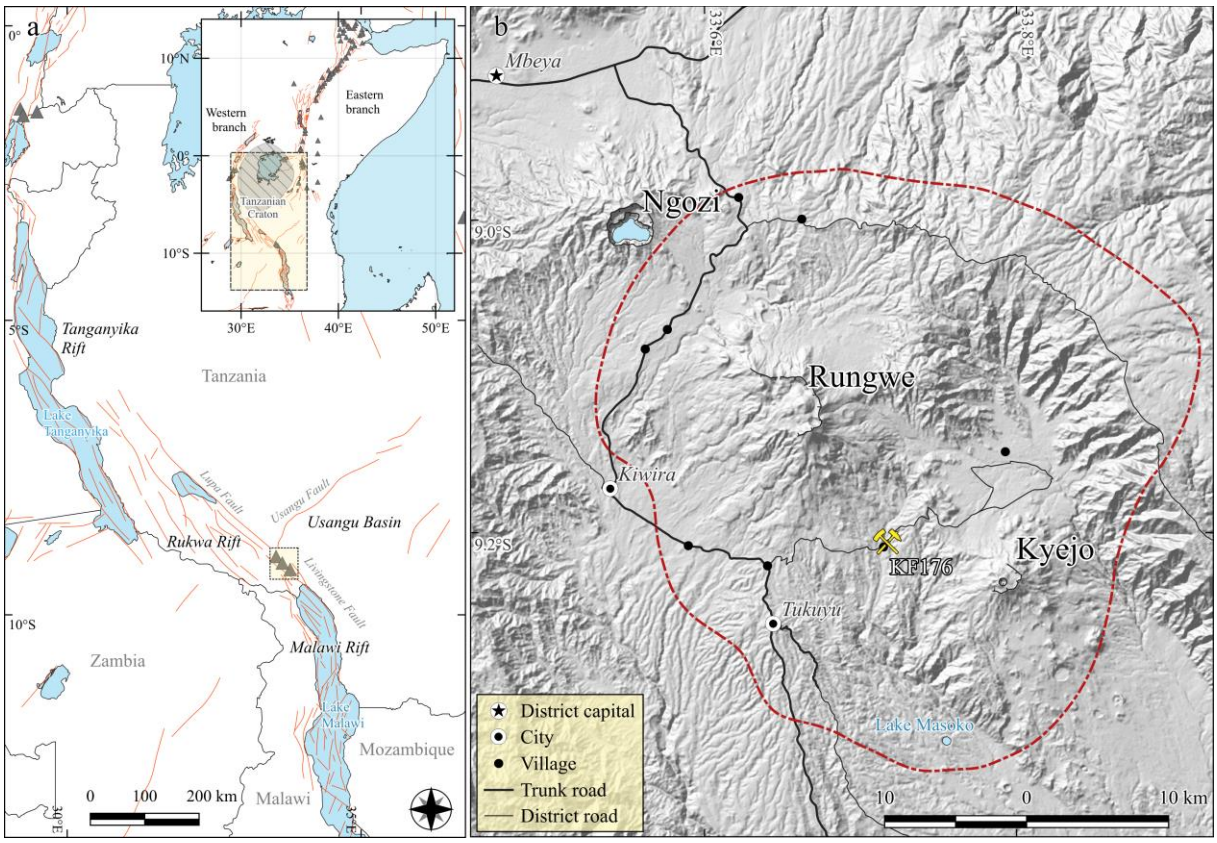

Fig. 2: Typical appearance of FTIR spectra for haüyne crystals and MIs volcanic glasses from our sample set. The main peaks for total water, molecular water, CO_2 and SO_4 are reported, while the inset zooms into the Near-IR region where the small molecular water and OH^- peaks are found.

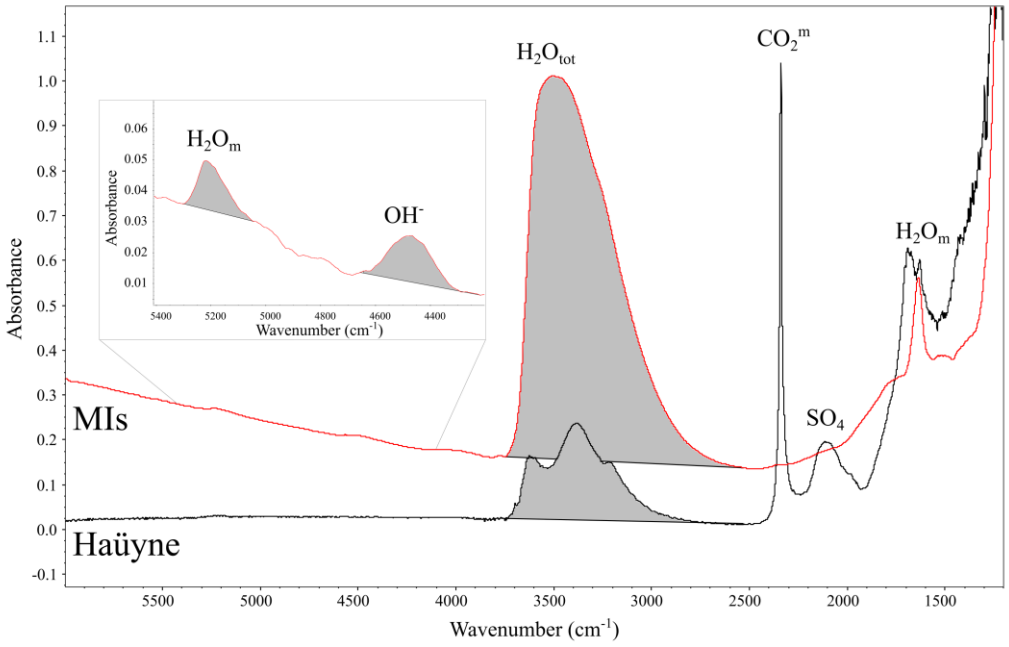

Fig. 3: Variations of componentry occurrence across the Rungwe Pumice deposit (*markers*). The top x-axis illustrates the cumulative distribution of the different crystalline phases (*bars*) within the crystal component. As the alkali feldspars always represent at least 80% of crystals, the axis origin was set at this value. For both, the medium and coarse ash grain sizes are reported separately.

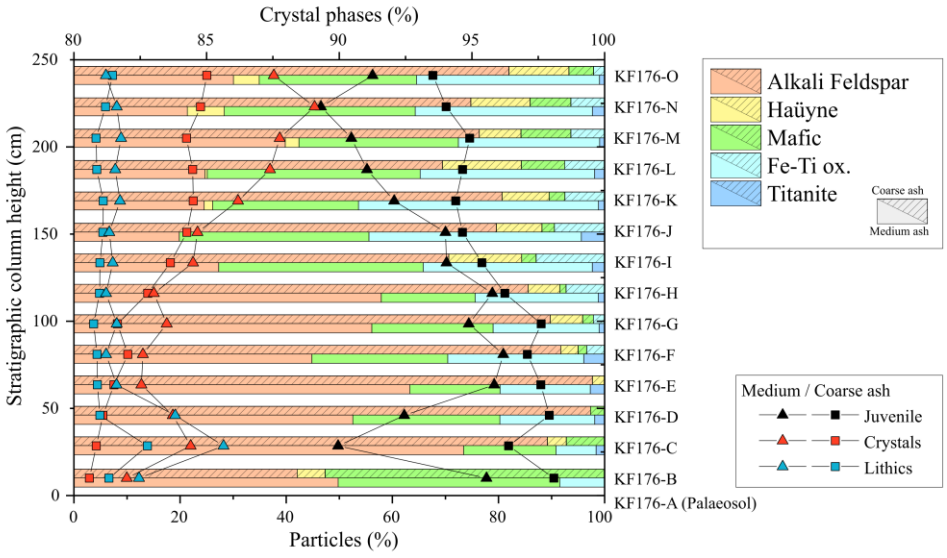

Fig. 4: Melt inclusion (MI) and embayment textures in haüyne crystals. **a)** Crystal hosting different types of MIs: e.g., ellipsoidal single-bubble or bubble-free MI and double-funnel embayment; **b)** funnel embayment; **c)** microvesicular MI hosting several larger bubbles; **d)** large, sub-planar, faceted MIs; **e)** elongated MIs hosting multiple bubbles of variable size; **f)** embayment hosting several large bubbles connected to the outside and microvesicular in its most internal portions; **g)** distributions of different types of MIs within the different horizons of the deposit; **h)** Box-and-whisker plot showing the statistical distribution of volume occupancy for the different types of MI-hosted bubbles. The *horizontal line* indicates the median, whereas the *asterisk* indicates the mean. *Whiskers* delimit 90% of the data set, whereas *circles* indicate outliers.

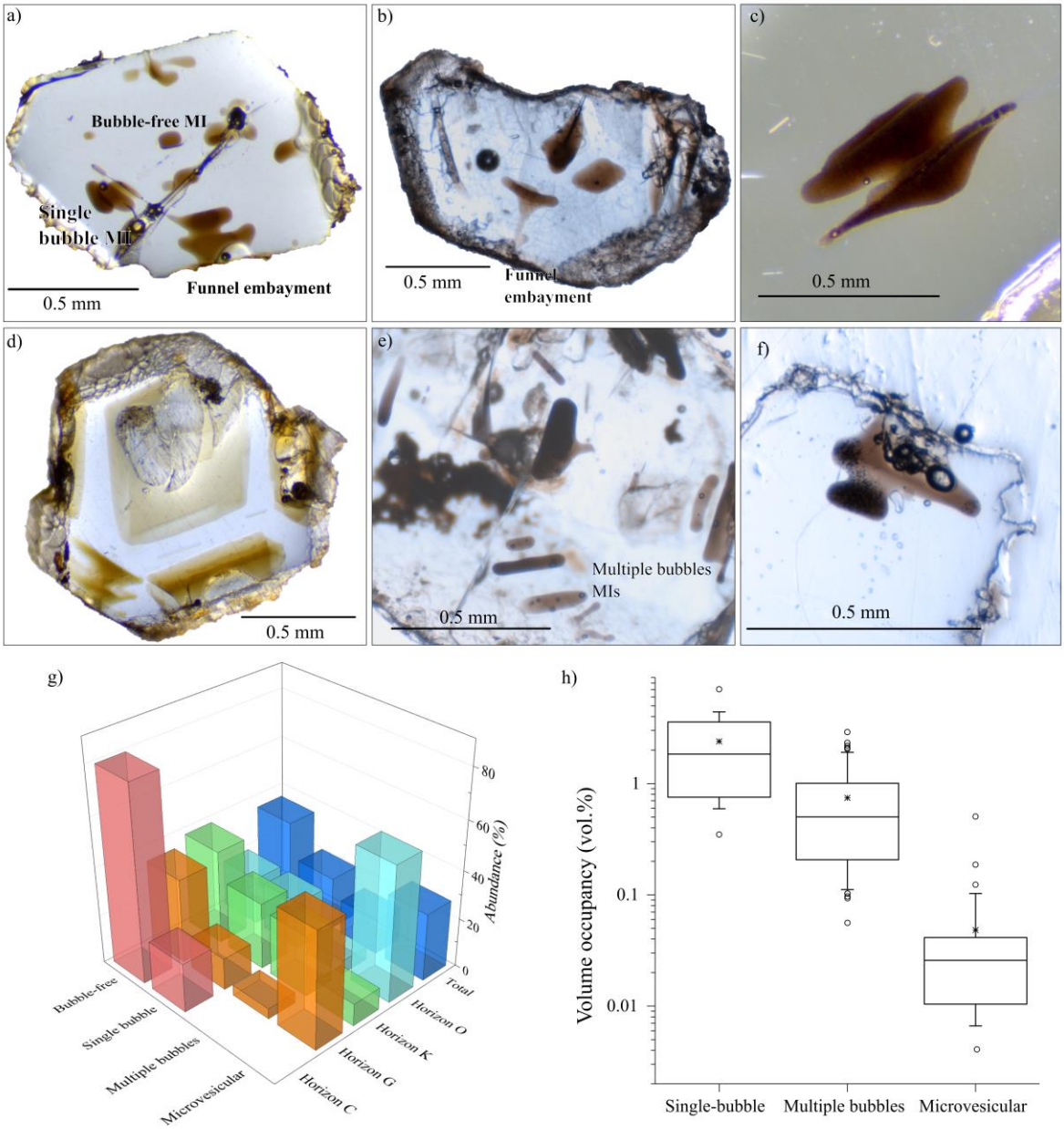

Fig. 5: **a)** Box-and-whisker plots of water concentrations within melt inclusions and embayments for the different horizons of the RP type section. The *horizontal line* indicates the median, whereas the *asterisk* indicates the mean. *Whiskers* delimit the maximum and minimum values within the dataset; **b)** Comparison between the water content estimated with the 3500 cm^{-1} overtone and the combination of the 4500 cm^{-1} and the 5200 cm^{-1} overtones.

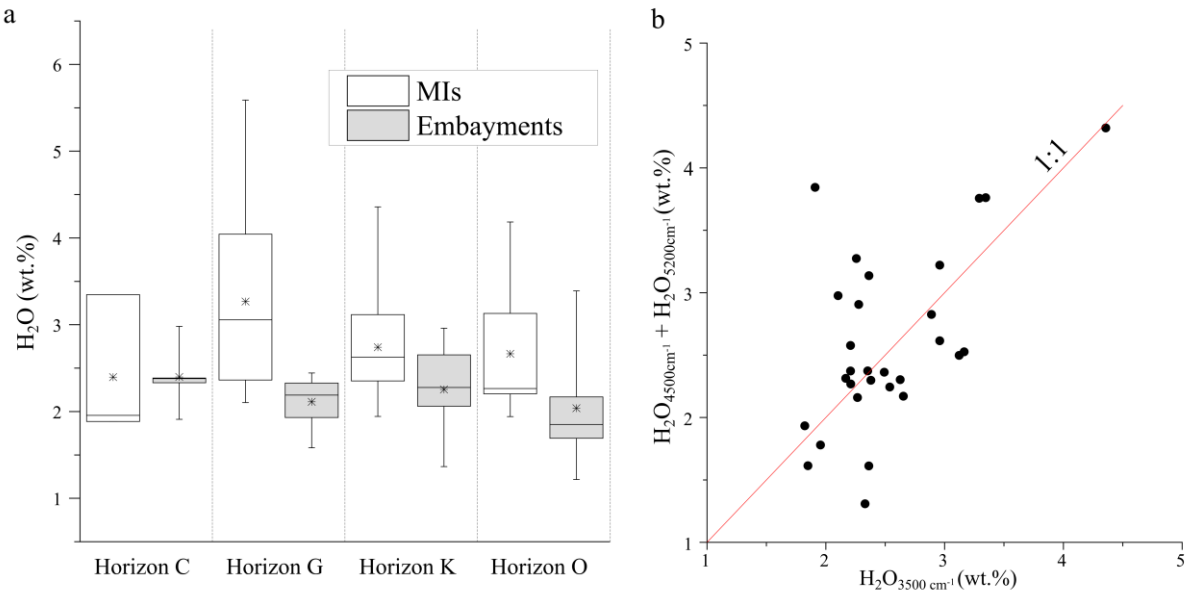

Fig. 6: **a**) Box-and-whisker plots of temperatures estimated for the melt inclusions (MIs) and embayments using the K-feldspar-liquid hygrometer (Mollo et al., 2015) and the alkali feldspar-liquid geothermometer (Putirka, 2008). The *horizontal line* indicates the median, whereas the *asterisk* indicates the mean. *Whiskers* delimit the maximum and minimum values within the dataset. *Grey dots* indicate the temperature values estimated for each MI; **b)** and **c)** *left axis*: Kernel density estimations comparing the minimum pressure values obtained by applying different solubility models: MagmaSat (Ghiorso and Gualda, 2015), MooreWater (Moore et al., 1998), Iacono-MarzianoWater (Iacono-Marzian et al., 2012) and ShishkinaWater (Shishkina et al., 2014). The *red dots* indicate the pressure values estimated with the MagmaSat solubility model separately for the different horizons of the deposit (*right axis*).

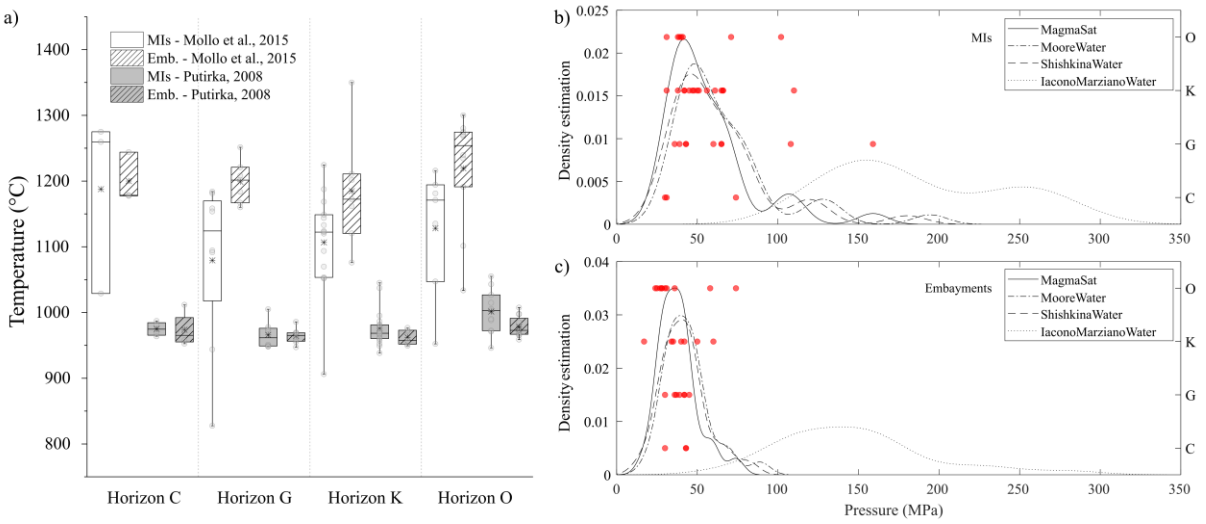

Fig. 7: Total alkali-silica diagram for the melt inclusions (including embayments), tephra matrix glass and pumice bulk rock compositions. The inset zooms in on the phonolite-trachyte field. *MI:* melt inclusions; *Tephra:* tephra glass matrix; *Bulk:* pumice whole rock.

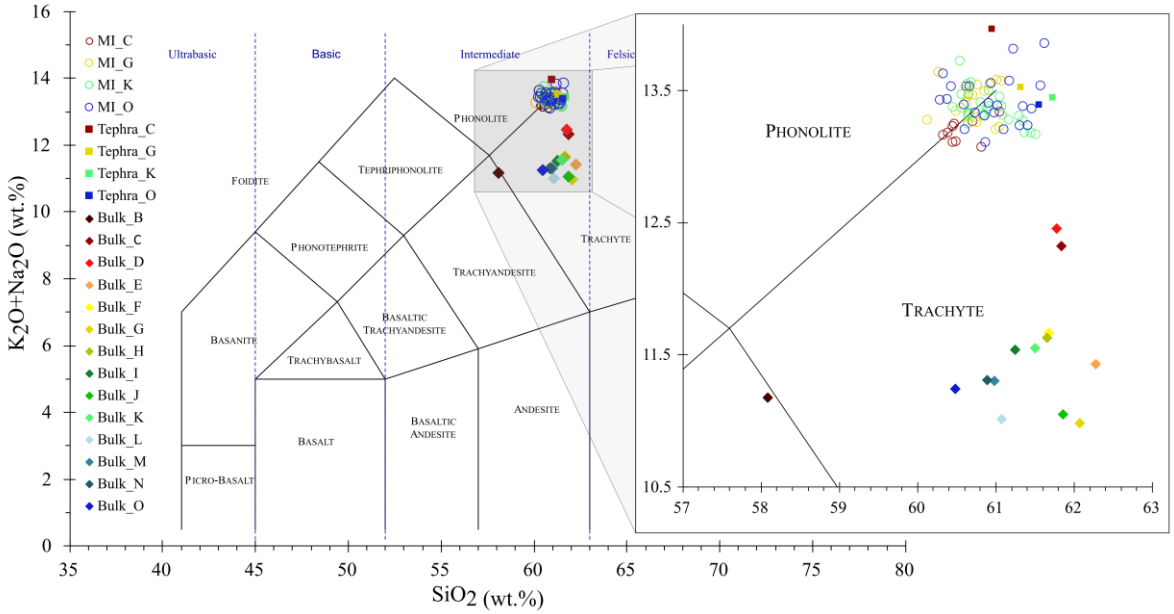

1603

1604

Fig. 8: **a)** and **b)** major element binary plots for melt inclusions and embayments, including geochemical data for melt inclusions hosted in different crystalline phases of Rungwe Pumice available in the literature (Fontijn et al., 2013); **c)** changes of major element concentrations across the deposit for melt inclusions, embayments and tephra matrix glass. The *red* and *blue* curves show mean values for each horizon for melt inclusions and embayments respectively.

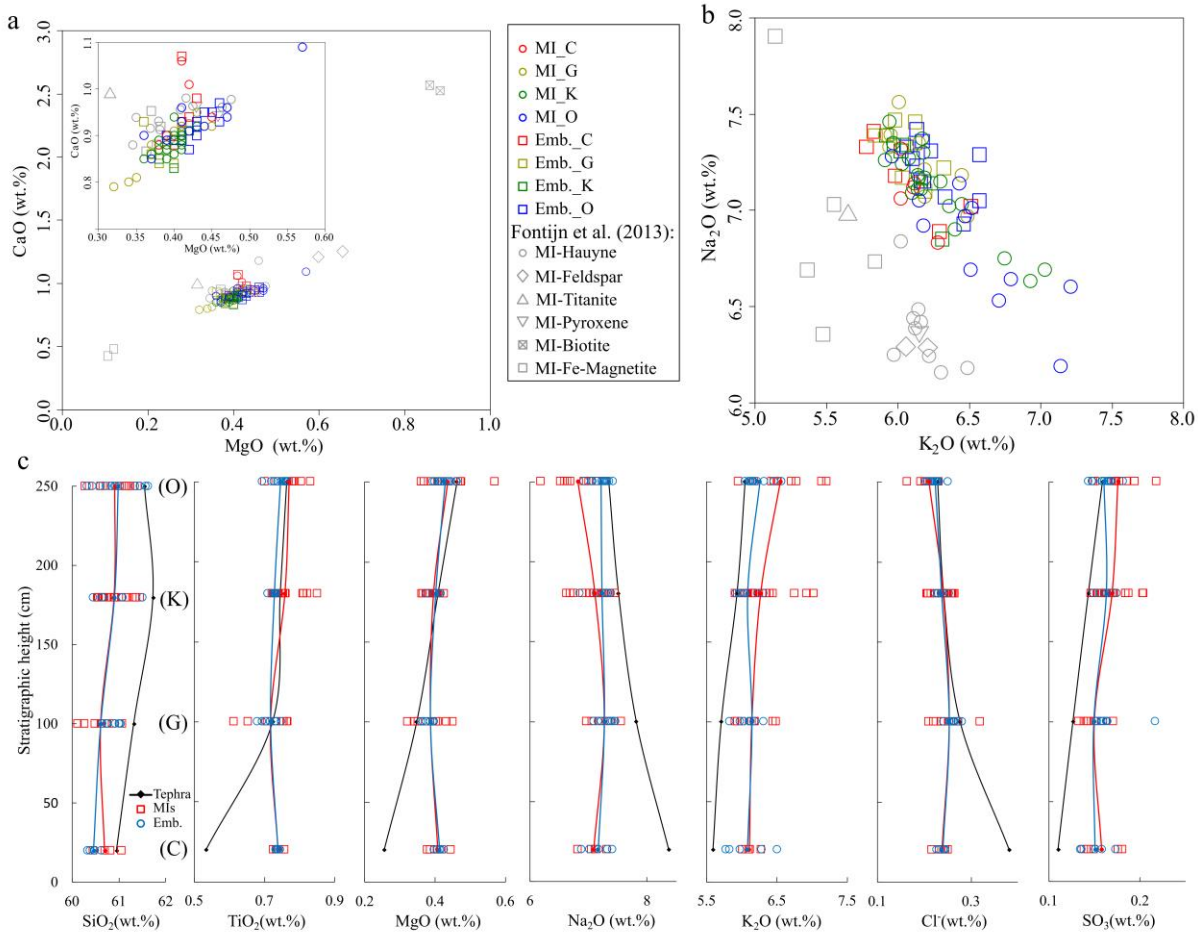

Fig. 9: Principal component analysis of major element concentrations: for each melt inclusion (including embayments) the values of the three major principal components obtained are shown together with the variance contribution of each element (*blue lines*). The samples were divided into two major clusters (*green and cyan ellipses*) plus an outlier (*red dot*) through hierarchical clustering. Statistical distribution of SiO_2, Na_2O, K_2O and H_2O concentrations for each cluster are shown in violin plots.

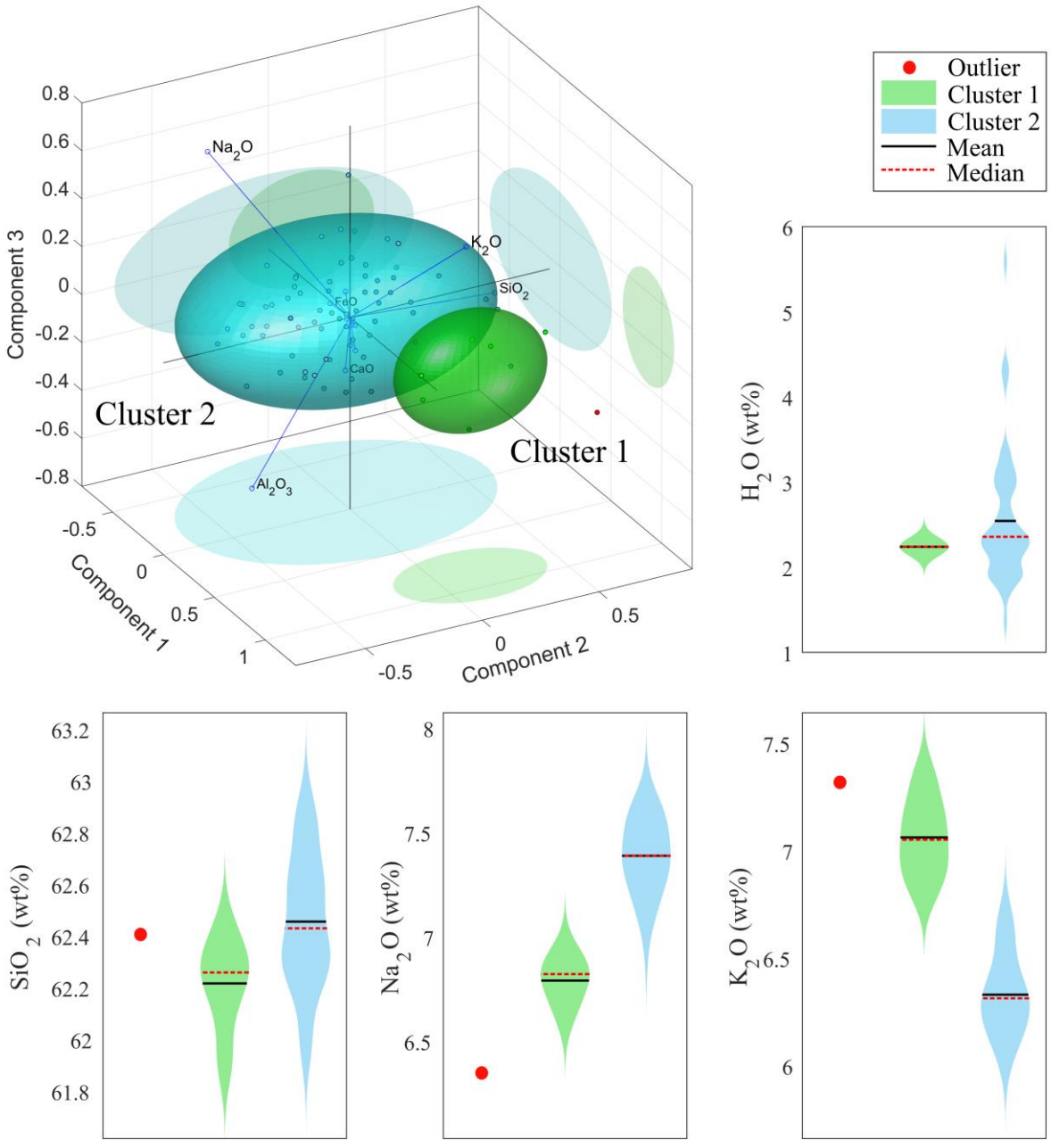

Fig. 10: Binary plots showing the liquid line of descent of major elements concentrations computed with rhyolite-MELTS (v. 1.0.2.; Gualda et al., 2012a; Ghiorso and Gualda, 2015) for a range of pressures and an initial water content of 0.3 wt.%. Values for melt inclusions (including embayments) are reported together with tephra matrix glass and values available in the literature for melt inclusions collected in different types of RP crystals (*grey symbols*; Fontijn et al., 2013). *Alk Flds - Alkali Feldspar; Biot – Biotite; Mgnt – Magnetite; Pyx – Pyroxene.*

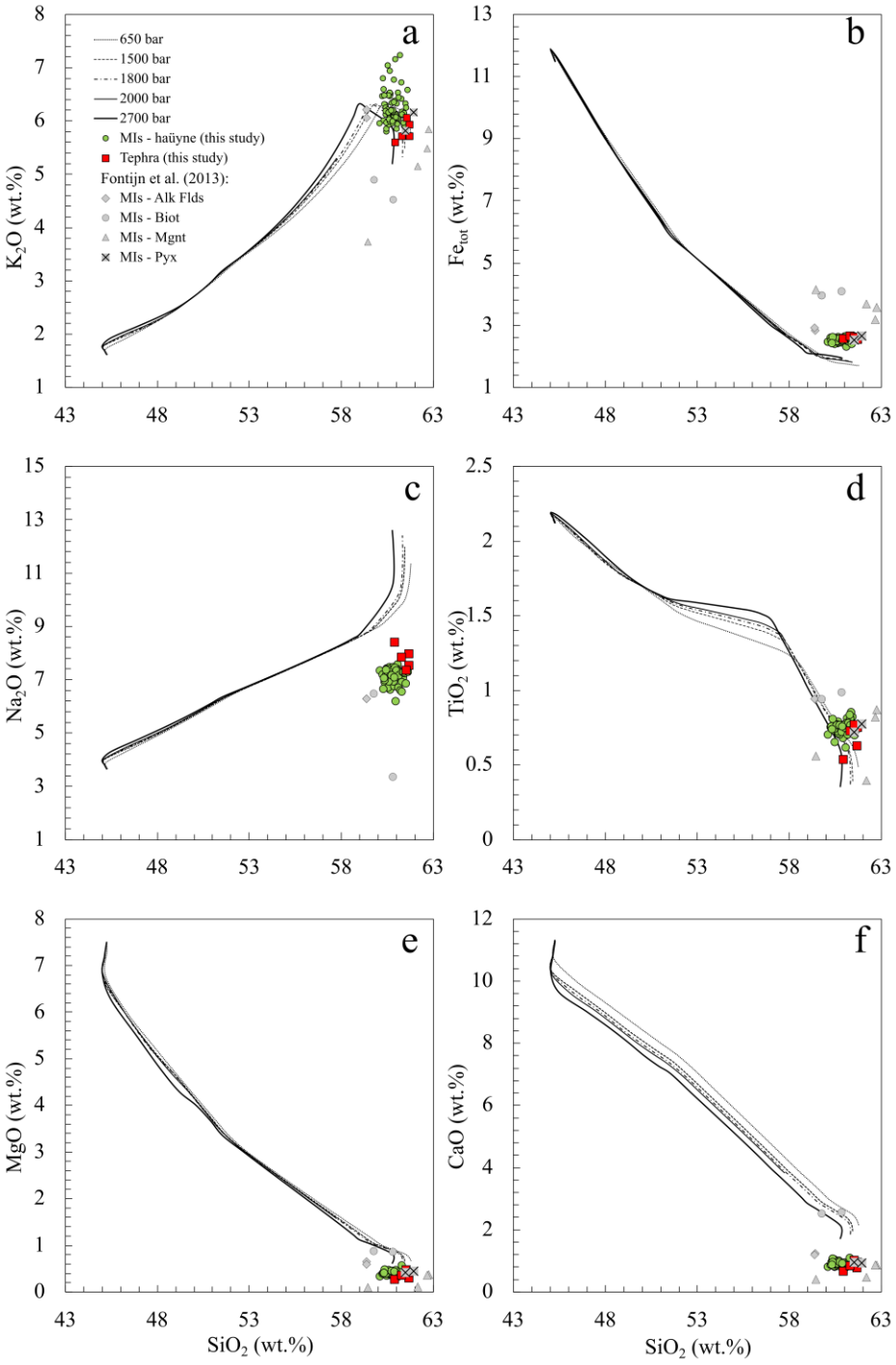

Fig. 11: a) Spider diagram of primitive mantle-normalised (McDonough and Sun, 1995) trace elements and **b)** REE for pumice bulk rock of the different stratigraphic horizons, compared to values available in the literature for RP pumice bulk rock (Fontijn et al., 2013) and for older Rungwe basalts (Castillo et al., 2014); **c)** comparison of the variation of concentration across the stratigraphic horizons for incompatible (i.e., increases from bottom to top of the magmatic reservoir; e.g., Zr) and compatible (i.e., decreases from bottom to top of the magmatic reservoir; e.g., Ba) trace elements. Hypothetical variations of element concentration as a function of fractional crystallisation (FC%) were computed assuming the horizon O as the less evolved (initial) liquid composition. Two cases were considered: the maximum (bulk partition coefficient, $D_{Zr} = 0$; *grey area*) and a lesser ($D_{Zr} = 0.3$; *yellow area*) incompatibility of Zr while the compatibility of Ba was made to change between $D_{Ba}=5$ and $D_{Ba}=25$. The bulk partition coefficient ranges were selected as the best areas enclosing data points after iterative attempts; **d)** comparison of the concentration variation across the stratigraphic horizons for two incompatible elements. A hypothetical FC trend was traced assuming a total incompatibility ($D = 0$) for both elements. The legend shared by all diagrams is shown in panel **c)**.

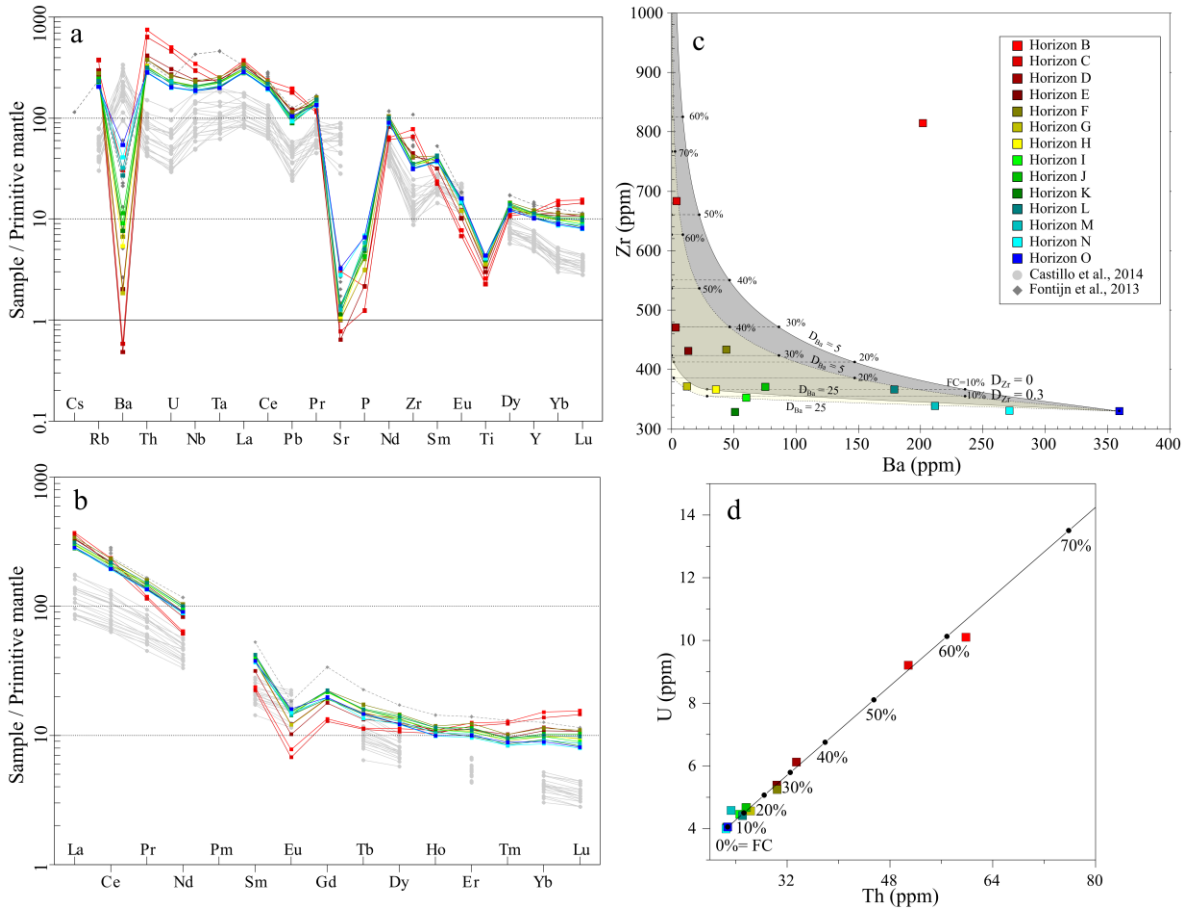

Fig.12: Comparison of major element oxide concentrations of bulk rock, pumice matrix glass and haüyne-hosted melt inclusions. For reference, compositions of MIs hosted in various mineralogical phases after Fontijn et al. (2013) are also reported.

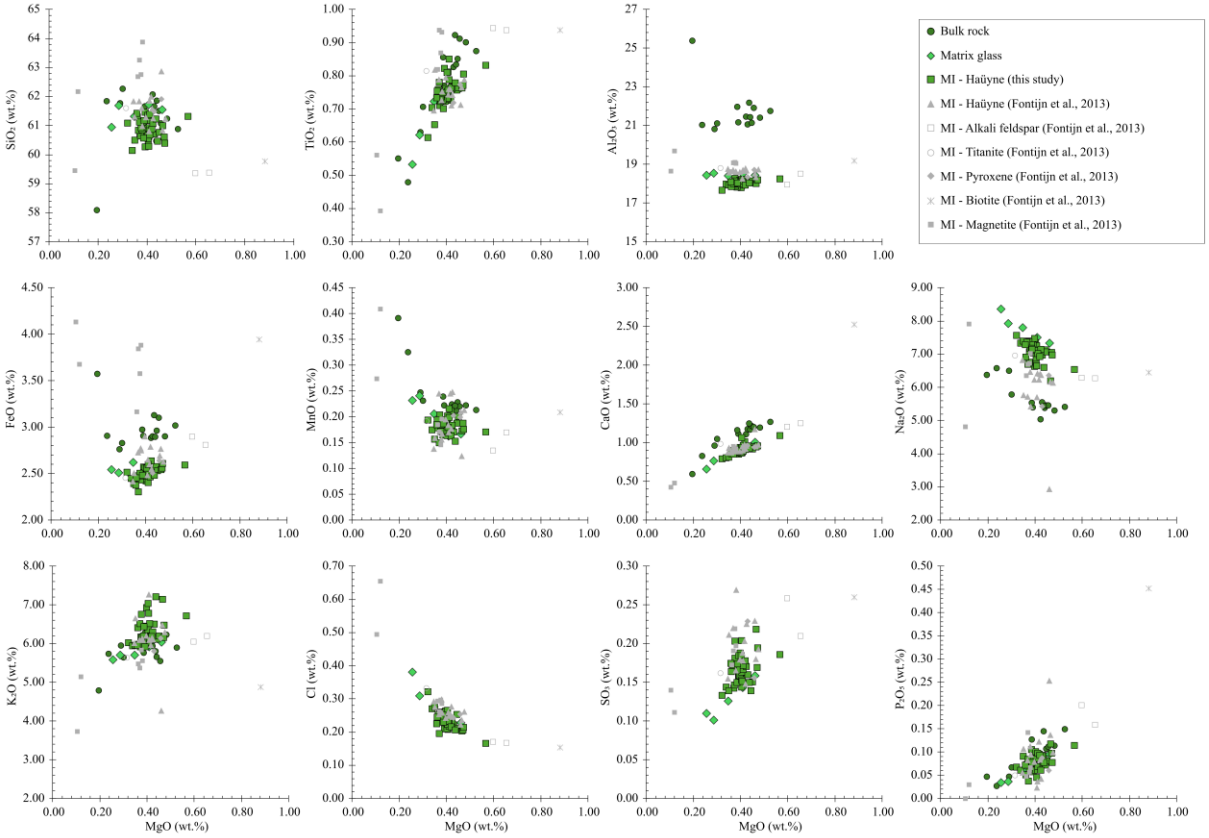

Fig.13: Schematic conceptual model of the proposed plumbing system dynamics pre-Rungwe Pumice eruption. **a)** A magmatic batch evolves at depth from a primitive magma of, presumably, basaltic composition forming a peralkaline trachytic magma. Early fractionation of biotite and pyroxenes occurs at a depth of up to 12 km (Fontijn et al., 2013); **b)** rising in the crust, alkali feldspars fractionation is promoted forming a crystalline mush at the reservoir bottom; **c)** gaseous phases sparging from depth promote haüyne crystallisation at shallow depths and shortly after trigger the eruption. The rising of a deep magmatic plume is unknown. An opening phase of reduced intensity involves a shallower and older reservoir, which experienced a different magmatic evolution; **d)** eventually, prolonged gas-sparing led to the Plinian-style eruption.

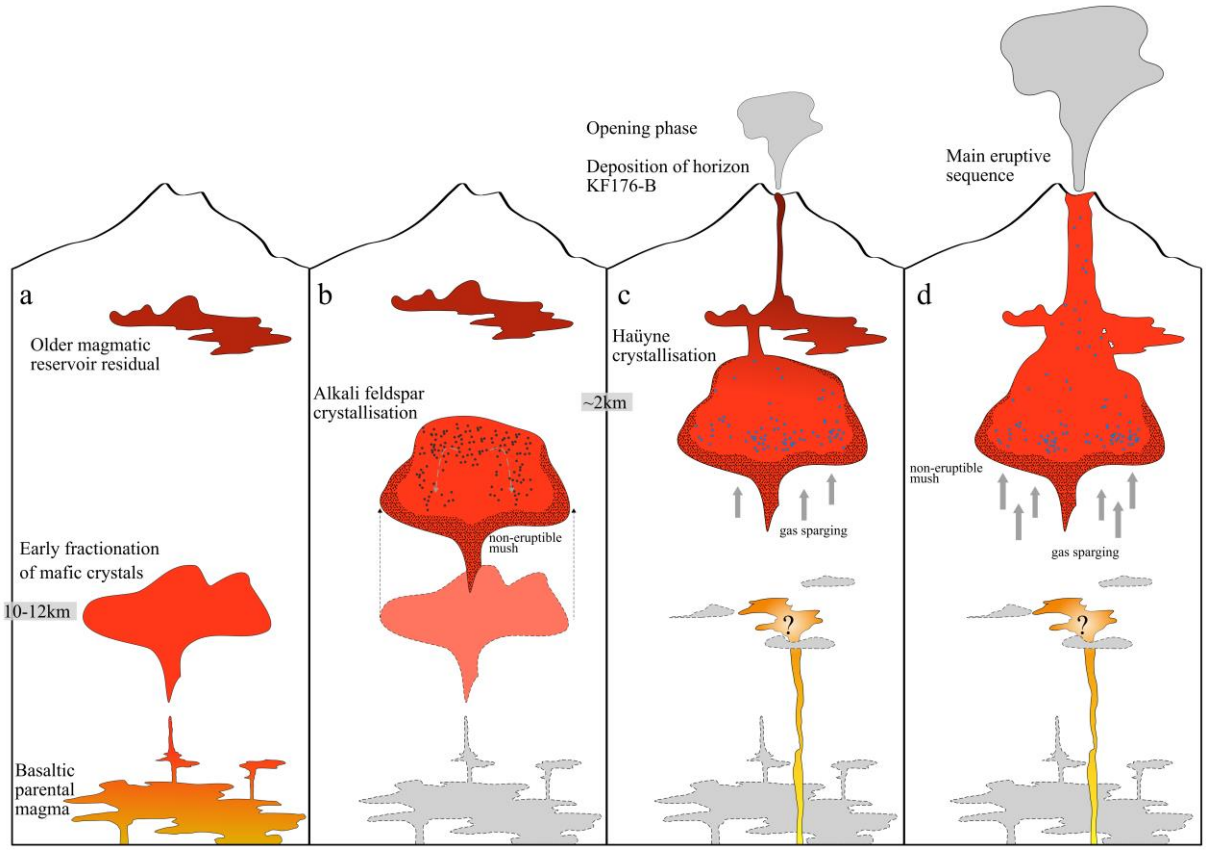

TABLES

Table 1

Major element compositions obtained with EPMA of pumice matrix glass of five different horizons of the Rungwe Pumice tephra deposit. Major and trace element composition of pumice bulk rock for the whole deposit were analysed with ICP-OES and Q-ICP-MS respectively. Bulk rock major element oxides are normalized to 100%. Lava flow basalt composition is also reported after Furman (1995).

Sample	Matrix glass					Bulk rock													Primitive basalt (Furman, 1995)
	KF176-C	KF176-D	KF176-G	KF176-K	KF176-O	KF176-B	KF176-C	KF176-D	KF176-E	KF176-F	KF176-G	KF176-H	KF176-I	KF176-J	KF176-K	KF176-L	KF176-M	KF176-N	KF176-O	RUN-2
wt.%																				
SiO_2	61.0	61.7	61.3	61.7	61.6	58.08	61.84	61.77	62.27	61.67	62.08	61.66	61.25	61.86	61.50	61.08	60.98	60.88	60.48	44.99
TiO_2	0.534	0.623	0.723	0.745	0.764	0.551	0.479	0.630	0.707	0.770	0.776	0.827	0.901	0.834	0.852	0.913	0.857	0.874	0.922	2.11
Al_2O_3	18.45	18.56	18.42	18.53	18.46	25.39	21.03	20.84	21.11	21.17	21.45	21.07	21.40	21.45	21.14	21.91	21.97	21.76	22.17	15.54
FeO	2.55	2.51	2.63	2.51	2.58	3.57	2.91	2.76	2.83	2.91	2.88	2.90	2.90	2.89	2.96	3.10	2.97	3.02	3.13	*12.38
MnO	0.233	0.242	0.207	0.163	0.168	0.392	0.326	0.248	0.231	0.222	0.224	0.219	0.222	0.213	0.228	0.221	0.240	0.214	0.222	0.19
MgO	0.26	0.29	0.35	0.41	0.46	0.20	0.24	0.29	0.30	0.39	0.42	0.43	0.48	0.44	0.45	0.46	0.39	0.53	0.44	7.45
CaO	0.66	0.77	0.84	0.94	1.01	0.59	0.83	0.96	1.05	1.11	1.11	1.17	1.20	1.17	1.21	1.20	1.16	1.27	1.25	11.22
Na_2O	8.37	7.94	7.82	7.51	7.34	6.38	6.58	6.50	5.78	5.39	5.05	5.55	5.30	5.39	5.45	5.46	5.54	5.40	5.44	3.64
K_2O	5.59	5.71	5.71	5.93	6.05	4.80	5.74	5.96	5.65	6.27	5.94	6.08	6.24	5.66	6.10	5.56	5.76	5.90	5.81	1.61
Cl	0.382	0.310	0.277	0.242	0.229															
SO_3	0.11	0.10	0.13	0.14	0.16															
P_2O_5	0.035	0.037	0.061	0.085	0.096	0.05	0.03	0.05	0.07	0.09	0.07	0.09	0.11	0.09	0.11	0.11	0.13	0.15	0.14	0.95
Total	98.12	98.78	98.47	98.92	98.86	*norm.*	*norm.*	*norm.*	*norm.*	*norm.*	*norm.*	*norm.*	*norm.*	*norm.*	*norm.*	*norm.*	*norm.*	*norm.*	*norm.*	100.08
H_2O (b.d.)	1.88	1.22	1.53	1.08	1.14															
LOI						6.97	6.09	5.79	6.43	6.87	7.70	6.77	7.87	7.23	6.91	8.06	8.00	7.77	8.35	
ppm																				
Sc						13.50	10.49	8.82	8.30	8.89	7.14	7.10	7.05	6.89	7.43	7.34	6.99	7.11	7.42	
V						6.32	22.92	10.22	20.65	16.94	21.70	12.01	23.55	16.59	33.38	12.75	25.08	14.15	18.85	
Cr						*bdl*	0.17	1.08	*bdl*	3.36	*bdl*	1.81	0.94	0.54	0.18	0.91	*bdl*	0.33	0.71	
Co						0.33	0.15	0.26	0.19	0.65	0.29	0.30	0.69	0.40	0.59	0.65	0.37	0.68	0.58	
Ni						*bdl*	*bdl*	*bdl*	*bdl*	*bdl*	*bdl*	*bdl*	*bdl*	*bdl*	*bdl*	*bdl*	*bdl*	*bdl*	*bdl*	
Cu						15.33	9.11	29.80	8.60	10.94	5.41	8.98	9.29	9.24	5.03	7.52	4.90	5.52	4.24	
Zn						175.71	115.40	100.73	79.74	86.25	68.83	104.11	74.57	79.63	81.91	79.25	73.83	71.48	70.45	
Ga						57.03	49.20	51.30	50.22	53.68	47.38	48.66	49.71	50.58	47.14	51.37	46.82	46.95	47.63	
Rb						179.08	225.89	177.70	163.26	166.19	145.02	145.69	141.47	148.61	133.17	140.89	123.87	124.83	122.65	
Sr						60.79	15.25	12.65	19.92	28.27	20.05	21.41	26.79	25.77	22.64	27.42	25.29	55.25	64.64	
Y						51.64	49.32	47.88	48.49	52.58	46.35	47.93	47.65	49.37	44.05	48.52	45.30	43.68	43.87	
Zr						814.60	683.68	471.29	431.77	434.09	371.99	366.71	353.08	370.99	328.65	366.56	338.92	331.12	330.09	
Nb						227.58	194.45	157.28	150.21	152.95	135.22	136.57	131.89	137.79	121.98	136.36	124.80	121.78	123.29	
Ba						201.52	3.83	3.17	13.35	43.91	12.21	35.37	59.77	75.27	50.64	178.75	211.14	271.03	359.20	
La						240.50	234.77	217.15	214.12	221.15	193.89	197.66	194.37	203.17	181.44	201.92	185.51	183.67	185.69	
Ce						395.08	345.25	364.91	368.51	392.78	347.20	361.03	349.06	368.15	330.03	365.79	337.09	322.46	327.38	
Pr						30.19	29.16	34.75	36.94	40.62	35.97	37.77	37.47	38.83	34.87	38.50	35.38	34.06	34.28	
Nd						80.15	77.00	103.37	114.27	129.81	113.25	122.11	121.44	125.67	111.73	125.23	112.36	110.11	113.31	
Sm						9.57	9.08	12.81	15.42	17.05	15.08	16.46	16.49	16.95	15.46	17.17	15.01	14.89	15.26	
Eu						1.20	1.04	1.57	1.88	2.20	1.86	2.29	2.27	2.38	2.21	2.35	2.23	2.30	2.47	
Gd						7.30	7.02	9.70	10.55	12.07	10.44	11.80	11.77	11.88	10.47	12.16	10.76	10.65	10.74	
Tb						1.12	1.11	1.32	1.46	1.71	1.49	1.55	1.58	1.58	1.44	1.56	1.44	1.34	1.46	
Dy						7.61	7.20	8.38	9.06	9.84	8.84	9.21	8.97	9.61	8.29	9.34	8.67	8.18	8.25	
Ho						1.64	1.54	1.65	1.59	1.76	1.67	1.72	1.65	1.71	1.59	1.72	1.56	1.47	1.48	
Er						5.49	5.16	4.83	4.96	5.41	4.69	4.78	4.60	5.01	4.31	4.82	4.49	4.20	4.37	
Tm						0.87	0.84	0.69	0.66	0.69	0.61	0.65	0.64	0.64	0.59	0.65	0.57	0.57	0.60	
Yb						6.69	6.05	5.10	4.77	5.02	4.33	4.39	4.30	4.55	4.08	4.42	4.05	3.80	3.93	
Lu						1.06	0.99	0.72	0.73	0.75	0.65	0.64	0.61	0.70	0.56	0.67	0.59	0.54	0.55	
Hf						15.16	13.10	9.41	8.59	8.71	7.55	7.36	7.19	7.58	6.51	7.43	6.79	6.41	6.46	
Ta						9.35	8.09	8.84	8.93	9.38	8.42	8.53	8.27	8.61	7.58	8.45	7.70	7.39	7.37	
Pb						29.29	26.79	18.09	17.03	17.21	14.69	14.90	14.37	15.17	13.43	14.49	14.01	13.96	15.71	
Th						59.84	50.87	33.45	30.40	30.46	26.31	25.69	24.64	25.59	22.61	25.07	23.28	22.50	22.75	
U						10.10	9.21	6.12	5.38	5.24	4.56	4.67	4.45	4.67	4.04	4.41	4.58	3.99	4.05	

norm. = total major elements normalised to 100%; bdl = below detection limit.

**Iron indicated as Fe_2O_3 in Furman (1995).*

SUPPLEMENTARY MATERIAL

Supplementary Table 1: Melt inclusions and embayment catalogue comprehensive of detailed descriptions of qualitative and quantitative features. (available upon request to lorenzo.cappelli@ulb.be).

Supplementary Table 2: Results for each thermometer and barometer used to estimate the reservoir conditions. A summary of each method used, and the combination of different thermometers and barometers is reported in "MIs and Embayments" sheet, together with the estimated storage depth for each. (available upon request to lorenzo.cappelli@ulb.be).

Supplementary Table 3: Chemistry data for melt inclusions, embayments, mineralogical phases and grey pumice glass. Results for the standards used as a reference for EPMA and mass spectrometry are also reported as well as the instrument conditions used for EPMA. (available upon request to lorenzo.cappelli@ulb.be).

Supplementary Figure 1: a) Feldspar ternary diagram reporting core and rim analyses of alkali feldspars. Phyton3 tool Thermobar (v.0.07; Wieser et al., 2022) was used for data plotting; **b)** SEM backscattered electron image of an alkali feldspar crystal showing no evident textural zonation. The *red line* indicates the core-to-rim transect of analyses. (*Wieser, P.E., Petrelli, M., Lubbers, J., Wieser, E., Özaydın, S., Kent, A.J.R., Till, C.B., 2022. Thermobar: An open-source Python3 tool for thermobarometry and hygrometry. Volcanica 5, 349–384. https://doi.org/10.30909/vol.05.02.349384*)